https://doi.org/10.5194/egusphere-2026-5158
Preprint. Discussion started: 22 September 2026

Global continental and oceanic emissions of atmospheric microplastics inferred from pattern-restricted Bayesian inversion

Ondřej Tichý[1], Václav Košík[1], Sabine Eckhardt[2], Nikolaos Evangeliou[2], and Václav Šmídl[1]

[1]Institute of Information Theory and Automation, Czech Academy of Sciences, Pod Vodarenskou vezi 4, Prague, 18200, Czech Republic
[2]Stiftelsen NILU (former Norwegian Institute for Air Research), Department of Atmospheric Climate Research (ATMOS), PO Box 100, Kjeller, 2027, Norway

Correspondence: Nikolaos Evangeliou (ne@nilu.no)

Abstract. In this paper, we present global atmospheric microplastic (MP) emissions calculated using remote deposition measurements, Lagrangian transport modelling and a pattern-restricted Bayesian inversion. Emissions were constrained using four source patterns representing agricultural activity, bare-soil, road dust, and oceanic resuspension. A Gibbs-sampling framework combined with an orthogonal transformation of the inverse problem was used to quantify posterior emissions and their associated uncertainties. We estimate annual atmospheric MP emissions to be 1.46×10^{18} particles y^{-1}, equivalent to 1001 ± 781 Gg y^{-1} for particles 5–250 μm. Oceanic emissions dominate the global budget, contributing 763 ± 611 Gg y^{-1}, while agriculture, road dust, and bare-soil resuspension contribute 170 ± 125, 51 ± 31, and 17 ± 14 Gg y^{-1}, respectively. Independent validation against global atmospheric MP observations gives a correlation coefficient of 0.57, with 50% of modelled values within one order of magnitude and only 12% as outliers. Restricting this comparison to only observations over the ocean, together with a sensitivity experiment in which marine emissions were strongly reduced, reveals that oceanic emissions are likely non-negligible. The measured size distribution further indicates a strong decoupling between particle number and mass, with the 10–25 μm fraction dominating particle-number emissions, but not emitted mass. Consequently, assumptions regarding particle size, density, and geometry affect global mass estimates significantly and explain the large spread observed in previously reported inventories. Our results provide an observation-constrained estimate of the global atmospheric MP budget, in which the accuracy of the emissions is supported by an independent comparison.

1 Introduction

Global plastics production continues to rise, increasing from 370.7 Mt in 2018 to 413.8 Mt in 2023, of which only 8.7% was circular, mostly through mechanical recycling (Plastics Europe, 2024). As plastics degrade and fragment, a portion enters the environment as microplastics (MPs), defined as particles smaller than 5 mm. While MPs are present in soils (Xu et al., 2024), aquatic systems (Kye et al., 2023), and a wide range of organisms (Li et al., 2025; Wang et al., 2022) including humans (Leslie et al., 2022; Saha and Saha, 2024), they may also enter the atmosphere, contributing to a global airborne MPs cycle. The ability of MPs to undergo long-range atmospheric transport (Tatsii

https://doi.org/10.5194/egusphere-2026-5158
Preprint. Discussion started: 22 September 2026

et al., 2023) is further supported by their detection in remote environments, including protected areas and national parks (Brahney et al., 2020), Siberia (Frank et al., 2025), or even polar regions (Bergmann et al., 2019; Evangeliou et al., 2020).

Despite the atmosphere being an important environmental compartment contaminated with MPs, it remains the least explored medium, largely due to difficulties in modelling their complex shapes and in measuring their macromolecular polymer composition. Once released into the environment, MPs undergo mechanical, radiative, chemical, and biological degradation that alters their size, shape, surface properties, composition, and overall mobility. These transformations make them prone to becoming airborne through surface turbulence, much like mineral dust, from both, land (Evangelou et al., 2024) and ocean surface (Allen et al., 2020). Recent studies (Brahney et al., 2021; Evangeliou et al., 2022; Fu et al., 2023; Yang et al., 2025) have identified that the key emitters of MPs are road dust originated from tire and brake wear, agricultural activity (plastic nets), resuspension from bare soils such as deserts, and resuspension from the surface of the ocean via bubble bursting and wave breaking into the shore (Jiang et al., 2025). Although Yang et al. (2025) argued that the ocean contributes only a negligible share to global MPs emissions, other studies suggest a much higher role (Trainic et al., 2020; Allen et al., 2020). Here, we include the ocean as a possible source of atmospheric MPs and we evaluate its contribution to the atmospheric burden above oceans using a set of independent observations (Evangelou et al., 2025).

In bottom-up approaches, emissions are typically estimated on the basis of local knowledge such as concentration in a given environment combined with, e.g., experimentally obtained resuspension coefficients or emission factors. Here, we follow a top-down approach in which ambient measurements are compared with model predictions with optimized emissions. We used one of the most complete, in the sense of spatial and temporal distribution, dataset of MPs wet and dry deposition from remote regions in West United States Brahney et al. (2020). To allow for MPs emission optimization, we model the relations between measurements and each possible source location using the atmospheric transport model FLEXPART version 11 Bakels et al. (2024), which has been designed to model non-spherical particles, taking into account shape corrections during gravitational settling for non-spherical shapes (Tatsii et al., 2023).

However, without additional constraints, such an inverse estimation problem would be highly ill-posed, as many different solutions could fit the observations (Tarantola, 2005; Brožová et al., 2025). To address this ambiguity, we used an inverse model for MPs emission optimization, in which MPs emissions are restricted to follow specific global patterns discussed above, namely road dust, agriculture, bare soils, and oceans. Even with this pattern-restricted inversion approach, uncertainties related to measurements, transport parameterizations, and atmospheric modelling are expected to remain substantial (Ganesan et al., 2014). To explicitly account for these uncertainties, we employ a Bayesian inversion framework in which all unknown parameters are estimated without extensive tuning. For parameter estimation, we adopt Gibbs sampling rather than a variational method, as Gibbs sampling has the important property of not underestimating posterior uncertainty (Tichý et al., 2020). The Gibbs sampling method is a statistical method that repeatedly draws values for each unknown parameter, allowing us to approximate complex

https://doi.org/10.5194/egusphere-2026-5158
Preprint. Discussion started: 22 September 2026

probability distributions and their uncertainties that would otherwise be very difficult to calculate directly (Casella and George, 1992; Chib and Greenberg, 1995), which further allows us to better capture the uncertainties in global MPs emission estimates. The results are compared with the latest global emission estimates for MPs (Brahney et al., 2021; Evangeliou et al., 2022; Fu et al., 2023; Yang et al., 2025; Evangelou et al., 2026), as well as emissions calculated for specific environmental compartments, such as from bare soils (Evangelou et al., 2024) or the ocean (Shaw et al., 2023; Harb et al., 2023; Bucci et al., 2024).

2 Measurements and atmospheric modelling

2.1 Measurements of dry and wet deposition

Measurements used in inverse modelling must be representative of the modelled spatiotemporal scales, have well-characterized and realistic uncertainty estimates, and be as free from systematic bias as possible, since inversions cannot distinguish observational bias from emission errors. They need sufficient temporal variability and coverage across different meteorological regimes to provide information on sources, and they must be sensitive to the emissions being inferred through transport and source-receptor matrix (SRM) diversity. Observations must also be consistent with the forward model in terms of units, definitions, averaging, and physical meaning, and be accompanied by adequate metadata and quality control so that representativeness, error correlations, and exclusions can be justified (Enting, 2002; Tarantola, 2005). Although not all of the aforementioned criteria are met with respect to atmospheric MP observations, the only public MP measurement dataset that is consistent enough to be used in inverse algorithm is from Brahney et al. (2020) in the sense that all samples were corrected and measured with the same techniques.

Brahney et al. (2020) collected dry and wet samples from the 11 remote ares and national parks in the Western USA. Specifically, the samples were collected using Aerochem Metrics model 31 wet/dry collectors between 2017 and 2019. The collectors were able to open and close dry and wet buckets based on a precipitation sensor. Field blanks, as well as laboratory open air and process blanks were routinely collected to assess the possibility of contamination and determine associated error. All samples were weighed and counted at 100x magnification using a BX50 Olympus Microscope and cellSens Imaging Software and were separated into five size classes (5-10 μm, 10-25 μm, 25-50 μm, 50-100 μm, and 100-250 μm), which allowed us to have a measured size distribution. Then, according to their observed shapes (e.g., 39% of particles less than 25 µm were spheres) they were converted to mass deposition rates. Mass deposition rates were also estimated using a Thermo Scientific^{TM} NicoletTM iN10 Fourier Transform Infra Red (FTIR) microscope using two different modes of analysis, reflection and micro-ATR (attenuated total reflectance). FTIR provides both the number of polymeric particles, as well as the area of the sample that was identified as polymeric, organic, or silicate. Both the count-based and the FTIR-based deposition estimates showed a strong relationship ($r = 0.89$, $p<0.001$), even though they differ slightly in magnitude, which gives credence to the deposition measurements and to how they relate to the drivers of plastic emissions to the atmosphere. From the whole dataset, we selected only those samples that were collected during year 2018 in order to perform a full year

https://doi.org/10.5194/egusphere-2026-5158
Preprint. Discussion started: 22 September 2026

top-down calculation of atmospheric MPs emissions. In addition, year 2018 is well covered by measurements while the remaining years (2017, 2019) are covered only partially. In total, we used 209 wet and 96 dry, with mean density of 1.22 $g \cdot cm^{-3}$ based on the detected polymers using the FTIR Brahney et al. (2020).

2.2 Atmospheric transport modelling

To calculate the SRMs, we used the upgraded Lagrangian particle dispersion model FLEXPART version 11 (hereafter FLEXPARTv11) (Bakels et al., 2024) driven with ERA5 assimilated meteorological data (Hersbach et al., 2020), which includes 137 vertical levels, hourly time resolution, and a spatial resolution of 0.5° x 0.5°. The SRMs were calculated in reverse time mode, utilizing a feature that reconstructs both wet and dry deposition at the receptor site for backward simulations (Eckhardt et al., 2017). Wet deposition of MPs was modelled by releasing computational particles at the receptor during precipitation events at altitudes of 0–20 km above sea level. For dry deposition, particles were released at a height of 0–30 m at the same receptor point, corresponding to the layer where particles experience dry deposition in forward mode. Each released particle represents a unit deposition amount, which was immediately converted to atmospheric concentrations based on the deposition intensity characterized by either dry deposition velocities or the wet scavenging rates (both in-cloud and below-cloud) (Grythe et al., 2017; Eckhardt et al., 2017). This process allows for the determination of sensitivities between emissions and deposition amounts for 50-day backward tracking based on the long atmospheric lifetimes of MPs (Evangeliou et al., 2020).

FLEXPARTv11 is of the most effective models for simulating MPs, as it uses shape corrections for gravitational settling of non-spherical shapes (Tatsii et al., 2023). Based on experiments showing that that non-spherical particles experience a larger drag in the atmosphere and therefore have lower settling velocities than volume-equivalent spherical ones, Tatsii et al. (2023) implemented and tested how non-spherical shapes affect FLEXPARTv11 transport. They reported that settling velocities for fibers can be less than one-third of those of spherical particles with the same volume, while fragments fall in between. In the present study, MPs were modelled as spheres (39%) and the rest (61%) as fragments to be exactly consistent with the findings reported by Brahney et al. (2020), while fibers were not modelled. Fragments were defined as cylinders with base diameters those measured by Brahney et al. (2020) and aspect ratios of 5, 10 and 20 (which determine the cylinder's length). Since the updates in FLEXPARTv11 involve only settling, while wet scavenging of non-spherical particles has not been measured yet, we also perturbed scavenging coefficients to calculate the sensitivity of the results to different scavenging coefficients for in-cloud and below-cloud. We used three MP species with cloud condensation nuclei (CCN) and ice nuclei (IN) efficiencies of 0.01 and 0.01 (low scavenging), 0.05 and 0.15 (medium scavenging), 0.35 and 0.55 (high scavenging), respectively.

https://doi.org/10.5194/egusphere-2026-5158
Preprint. Discussion started: 22 September 2026

3 Inverse modelling

3.1 Standard methods

We utilize the concept of the SRM between the source and measurements, by Seibert and Frank (2004), which has been widely applied in atmospheric inverse modelling for continental-scale scenarios, including our study. This approach models the relationship between a potential emission source and a measurement, defined by its spatial coordinates and time interval, as the sensitivity of that measurement to a unit release, as simulated by an atmospheric transport model.

For each source location, we calculate SRMs for each measurement and potential emission time step constructing the coefficient $\widetilde{m_{i,j}}$ for every measurement y_i and emission time step j, and forming the SRM $\widetilde{\boldsymbol{M}}$. Given a measurement vector $\boldsymbol{y}$ and an emission vector $\widetilde{\boldsymbol{x}}$, we express their relationship as:

$$\boldsymbol{y} = \widetilde{\boldsymbol{M}}\widetilde{\boldsymbol{x}} + \boldsymbol{e}, \tag{1}$$

where $\boldsymbol{e}$ represents the error term. The objective is to estimate the unknown emissions $\widetilde{\boldsymbol{x}}$ from this linear system.

While this formulation may be straightforward, real-world applications are naturally subject to uncertainty in all model components. For instance, measurement data, $\boldsymbol{y}$, contain observational noise and errors, the SRM, $\widetilde{\boldsymbol{M}}$, is affected by approximations in the atmospheric transport model and meteorological reanalyses used (Leelőssy et al., 2017; De Meutter and Delcloo, 2022).

In an idealized setting where $\widetilde{\boldsymbol{M}}$ is exactly known and $\boldsymbol{e}$ is negligible, a simple least-squares solution could be used to estimate emissions $\widetilde{\boldsymbol{x}}$. However, in practice, atmospheric transport models introduce biases caused by, e.g., approximations and parameterizations (Bocquet, 2012; Ganesan et al., 2014; Ling et al., 2021) and measurement networks provide incomplete and noisy observations. These factors make a direct least-squares solution unstable or even meaningless, as it amplifies errors and fails to provide physically meaningful solutions. Consequently, more sophisticated approaches incorporating uncertainty quantification and regularizations are necessary to obtain robust and reliable emission estimates (Tarantola, 2005; Ganesan et al., 2014; Brožová et al., 2025).

The inverse problem of emissions estimation from a point source is already challenging due to uncertainties in atmospheric transport modelling, measurement noise, and the limited spatial coverage of observations. However, when extending the inversion to a spatiotemporal domain, the problem becomes even more ill-conditioned (Eckhardt et al., 2023; Vojta et al., 2024; Brožová et al., 2025). In this case, a number of spatiotemporal distributions of the emissions can be considered with almost identical measurements fits, making it impossible to distinguish between possible solutions. This ill-posedness arises because even small variations in the timing and location of the emissions can lead, by coupling it to an atmospheric transport model, to similar measurement predictions. This may result in reconstructed concentrations that are highly sensitive to modelling errors and observational uncertainties. As a consequence, there is a strong need for additional constraints or regularizations.

https://doi.org/10.5194/egusphere-2026-5158
Preprint. Discussion started: 22 September 2026

Therefore, here we assumed that MPs emissions follow spatial patterns associated with known MPs source categories (see Section 3.2), rather than resolving individual emission sources explicitly. We used unit-less source patterns to regularize the possible source emissions on a global grid, so that we estimate monthly weights of each pattern instead of estimating each map element separately. This approach reduces the dimensionality of the inverse problem from emissions at individual grid cells to monthly weights of the prescribed source patterns.

3.2 Pattern-restricted inverse model

Similarly to previous studies (Brahney et al., 2021; Evangeliou et al., 2022), we assumed that atmospheric MPs originate mainly from four different global source sectors. This assumption was primarily motivated by the lack of consistent long-term observations over a global domain and served as regularization of the inverse problem. The four source sectors were (a) emissions from agricultural nets used in crop production, (b) resuspension from bare soils, (c) road dust, and (d) resuspension from ocean's surface. All these source categories have been previously identified as the main global sources of atmospheric MPs (Brahney et al., 2021; Evangeliou et al., 2022; Fu et al., 2023; Yang et al., 2025).

The agricultural pattern was adopted from Potapov et al. (2022) in which cropland land-cover was derived from satellite data. The cropland is unevenly distributed between global regions, with 55% in Eurasia, 17% in Africa, 16% in North and Central America, 9% in South America and 3% in Australia and Oceania. The pattern for bare soil resuspension was adopted from the FLEXDUST model (Groot Zwaaftink et al. (2017)) after simulating the full year with the most recent assimilated meteorological fields from ERA5 (Hersbach et al., 2020). Road dust source pattern has been used before (e.g., in (Evangeliou et al., 2020, 2022)) and was adopted here from the ECLIPSEv6b (Evaluating the Climate and Air Quality Impacts of Shortlived Pollutants version 6b) emission inventory (Klimont et al., 2017) after bottom-up calculations performed by IIASA (International Institute for Applied Systems Analysis) using the GAINS model (Greenhouse Gas and Air Pollution Interactions and Synergies). Finally, the pattern for oceanic resuspension was taken from Isobe et al. (2021) as gridded monthly surface concentration data, assuming that oceanic emissions of atmospheric MPs follow the same pattern as surface concentrations. In Isobe et al. (2021), data from several research projects conducted from 2000 to 2019 were used to create data on the oceanic abundance of MPs. The data has been corrected to wind speed and wave height and interpolated to the monthly gridded surface concentration data (Kako et al., 2011). For ocean surface emissions, we performed a correction for seasonal snow and sea-ice extent using data adopted from the ERA5 (Hersbach et al., 2023), assuming that atmospheric MPs are not resuspended from snow and sea-ice surfaces (Supplementary Information Figure S1). In fact, this is reasonable since in cold environments, plastic degradation slows down, leading to temporal accumulation of MPs and associated chemical pollutants, that can be released to the aquatic environment upon melting (Zhang et al., 2023; Edo et al., 2025). The annual average patterns for the aforementioned sources are shown in Figure S2.

https://doi.org/10.5194/egusphere-2026-5158
Preprint. Discussion started: 22 September 2026

The concept of SRM is modified here for four source sectors. The modified SRM for each source is calculated as:

$$\boldsymbol{M}_{\text{pattern}} = \sum_{\text{lat,lon}} \boldsymbol{S}_{\text{lat,lon}} \widetilde{\boldsymbol{M}}_{\text{lat,lon}}, \tag{2}$$

where $\boldsymbol{S}_{\text{lat,lon}}$ is normalized source activity at given location, see Figure S2, and $\widetilde{\boldsymbol{M}}_{\text{lat,lon}}$ is SRM calculated for each measurement and time-step at given location. The spatial activity fields $S_{\text{lat,lon}}$ are normalized by their maximum value (i.e., $\max S_{\text{lat,lon}} = 1$), so that they represent only the relative spatial distribution of emissions within each source pattern. Since the measurements are the mixture signal from all four considered sources, we aggregate these modified SRM from all considered source as:

$$\boldsymbol{M} = [\boldsymbol{M}_1, \boldsymbol{M}_2, \boldsymbol{M}_3, \boldsymbol{M}_4]. \tag{3}$$

Then, the modified inverse problem is formulated as follows:

$$\boldsymbol{y} = \boldsymbol{M}\boldsymbol{x}, \tag{4}$$

where $\boldsymbol{y} \in \mathbf{R}^p$ is the original measurement vector, $\boldsymbol{M} \in \mathbf{R}^{p \times n}$ is the modified SRM, and $\boldsymbol{x} \in \mathbf{R}^n$ is the vector containing the source-pattern weights over the considered time steps. This approach follows the pattern of each source but dramatically reduces the number of unknowns, vector $\boldsymbol{x}$, to be estimated.

3.3 Uncertainty Estimation using Gibbs sampling

The linear model (Eq. 4) is, in principle, inaccurate, and the goal of the inversion is to minimize the residues. However, due to model and measurement uncertainties, the minimum-residual solution is not unique, and solutions with slightly higher residuals may also be consistent with the observations. The aim of uncertainty estimation is to find a set of possible solutions. A probabilistic approach represents the residue as a random variable with a chosen distribution. Gaussian distribution is a common assumption on the residues, yielding a probabilistic model:

$$p(\boldsymbol{y}|\boldsymbol{M},\boldsymbol{x}) = \mathcal{N}(\boldsymbol{M}\boldsymbol{x}, \omega_y^{-1} I_p)$$

where I_p is the identity matrix of the given size equal to the number of measurements and the variance of the residues ω_y^{-1} is identical for all measured data. The assumptions about the source term are summarized in the form of a prior distribution:

$$p(\boldsymbol{x}) = t\mathcal{N}(\mathbf{0}, \omega_x^{-1} I_n, [0, +\infty]),$$

where ω_x^{-1} is the estimated variance of the emissions. Note that the prior is not a standard Gaussian distribution but its truncated version, assigning zero prior probability to negative values.

The posterior distribution of the source term is proportional to the product of the likelihood and the prior:

$$p(\boldsymbol{x}|\boldsymbol{M},\boldsymbol{y}) \propto \exp\Big(-\frac{1}{2}\omega_y(\boldsymbol{y}-\boldsymbol{M}\boldsymbol{x})^\top(\boldsymbol{y}-\boldsymbol{M}\boldsymbol{x}) - \frac{1}{2}\omega_x \boldsymbol{x}^\top \boldsymbol{x}\Big)\chi(\boldsymbol{x} > 0). \tag{5}$$

https://doi.org/10.5194/egusphere-2026-5158
Preprint. Discussion started: 22 September 2026

The presence of the positivity constraint makes the problem analytically intractable, requiring approximate solutions. We propose to use the Gibbs sampler for this task.

The Gibbs sampler is a type of Markov Chain Monte Carlo (MCMC) method that generates a sequence of samples consistent with the posterior distribution. The method is applicable to multivariate distributions $\boldsymbol{x} = [x_1, x_2, \ldots, x_n]$, for which it is possible to sample from conditional distributions for every dimension:

$$x_i \sim p(x_i | \{x_j, \forall j \neq i\}). \tag{6}$$

The key advantage of the method is its efficiency, which is achieved at the cost of the need for exact evaluation of the conditionals (Eq. 6).

Application of the Gibbs sampling to the unconstrained linear Gaussian problem (Eq. 4) is a textbook example, since all conditional samples are analytically tractable. However, the atmospheric inversion model has two specific features: i) positivity constraint, and ii) an ill-conditioned matrix M. We propose to address the latter using an orthogonal transformation of the linear model.

3.4 Orthogonal transformation

Standard Gibbs sampling can be inefficient when variables are highly correlated (see Figure S3). The problem may be avoided by rotating the coordinate system so that the components are independent. In our case, rotating the coordinate system can be done using the SVD (Singular Value Decomposition) decomposition of $\boldsymbol{M}$ matrix, i.e. $\boldsymbol{M} = \boldsymbol{U}\boldsymbol{\Lambda}\boldsymbol{V}^\top$. The problem is then reparametrized to:

$$\boldsymbol{y} = \boldsymbol{M}\boldsymbol{x} = \boldsymbol{A}\boldsymbol{\alpha},$$

where $\boldsymbol{A}$ is a transformation of the SRM, and $\boldsymbol{\alpha}$ is the new unknown variable:

$$\boldsymbol{A} = \boldsymbol{U}\boldsymbol{\Lambda} \qquad \boldsymbol{\alpha} = \boldsymbol{V}^\top \boldsymbol{x} \qquad \boldsymbol{x} = \boldsymbol{V}\boldsymbol{\alpha}. \tag{7}$$

Under this transformation, the joint distribution Eq. (5) changes to

$$p(\boldsymbol{\alpha}|\boldsymbol{A}, \boldsymbol{y}) \propto \exp\Big(-\frac{1}{2}\omega_y (\boldsymbol{y} - \boldsymbol{A}\boldsymbol{\alpha})^\top (\boldsymbol{y} - \boldsymbol{A}\boldsymbol{\alpha}) - \frac{1}{2}\omega_x \boldsymbol{\alpha}^\top \boldsymbol{\alpha} \Big) \chi(\boldsymbol{V}\boldsymbol{\alpha} > 0).$$

While the analytical solution of the unconstrained transformed problem is also available, the complication arises in sampling positive samples. We decompose the problem into individual dimensions as follows:

$$A\boldsymbol{\alpha} = \boldsymbol{a}_i \alpha_i + A_{/i}\boldsymbol{\alpha}_{/i}$$

where α_i is the ith element of vector $\boldsymbol{\alpha}$, $\boldsymbol{a}_i$ denotes the ith column of matrix A, and $a_{/i} = [a_1, a_2 \ldots, a_{i-1}, a_{i+1}, \ldots a_n]$ is the complement of the ith element, and $\boldsymbol{A}_{/i}$ is matrix A without the ith column. In similar fashion, we decompose $\boldsymbol{V}\boldsymbol{\alpha}$ into $\boldsymbol{V}\boldsymbol{\alpha} = \boldsymbol{v}_i \alpha_i + \boldsymbol{V}_{/i}\boldsymbol{\alpha}_{/i} = \boldsymbol{v}_i \alpha_i + \beta_i$ where $\boldsymbol{v}_i$ is the ith column of matrix $\boldsymbol{V}$ and $\beta_i = \boldsymbol{V}_{/i}\boldsymbol{\alpha}_{/i}$.

https://doi.org/10.5194/egusphere-2026-5158
Preprint. Discussion started: 22 September 2026

This parametrization yields the following inversion problem:

$$p(\alpha_i|\tilde{\boldsymbol{y}},\boldsymbol{A},\boldsymbol{\alpha}_{/i}) \propto \exp\Big(-\frac{1}{2}\omega_y(\tilde{\boldsymbol{y}}-\boldsymbol{a}_i\alpha_i)^\top(\tilde{\boldsymbol{y}}-\boldsymbol{a}_i\alpha_i) - \frac{1}{2}\omega_x\alpha_i^\top\alpha_i\Big)\chi(\boldsymbol{v}_i\alpha_i > -\boldsymbol{\beta}_i)$$

where $\tilde{\boldsymbol{y}} = \boldsymbol{y} - A_{/i}\boldsymbol{\alpha}_{/i}$. This problem allows analytical solution:

$$p(\alpha_i|\boldsymbol{y},\boldsymbol{M},\boldsymbol{\alpha}_{/i}) = t\mathcal{N}\left(\mu_i,\sigma_i^2,[c_i,d_i]\right) \tag{8}$$
$$\mu_i = \omega_y\tilde{\boldsymbol{y}}^\top\boldsymbol{a}_i\sigma_i^2,$$
$$\sigma_i^2 = \left(\omega_y\boldsymbol{a}_i^\top\boldsymbol{a}_i+\omega_x\right)^{-1}.$$
$$c_i = \max_{j\in(j:v_{i,j}>0)}\{-\beta_{i,j}/v_{i,j}\}$$
$$d_i = \min_{j\in(j:v_{i,j}<0)}\{-\beta_{i,j}/v_{i,j}\}$$

which is ready to be used in the Gibbs sampler.

3.5 Precision terms and final algorithm

The variable ω_x is the precision of the prior distribution on $\boldsymbol{x}$. It controls the strength of the regularization applied to $\boldsymbol{x}$. A larger ω_x implies a stronger prior belief that $\boldsymbol{x}$ should be close to zero. We choose a Gamma prior for ω_x as

$$p(\omega_x) = \Gamma(\epsilon_0,\epsilon_0), \qquad p(\omega_y) = \Gamma(\epsilon_0,\epsilon_0),$$

where ϵ_0 is a small number chosen for numerical stability. In our case, $\epsilon_0 = 10^{-10}$. The conditional posterior distribution is:

$$p(\omega_x|\boldsymbol{x}) \propto p(\boldsymbol{x}|\omega_x)p(\omega_x)$$
$$p(\omega_y|\boldsymbol{x},M,\boldsymbol{y}) \propto p(\boldsymbol{y}|\omega_y,\boldsymbol{M},\boldsymbol{x})p(\omega_y)$$

which has solution using the parametrization (Eq. 7):

$$\omega_x \sim \Gamma\left(\epsilon_0+\frac{n}{2},\epsilon_0+\frac{1}{2}\|\boldsymbol{\alpha}\|^2\right). \tag{9}$$
$$\omega_y \sim \Gamma\left(\epsilon_0+\frac{p}{2},\epsilon_0+\frac{1}{2}\|\boldsymbol{y}-\boldsymbol{A}\boldsymbol{\alpha}\|^2\right). \tag{10}$$

The final algorithm of the Gibbs sampler is summarized in Algorithm 1. The main modification from a classical Gibbs sampler is the reparametrization of the problem using orthogonal decomposition, which allows the conditional distribution to be expressed in a numerically stable form. The main consequence is the calculation of the limits for the truncated normal distribution in Eq. (8). The Normal distribution can be truncated from both sides, since vector $\boldsymbol{v}_i$ may contain negative entries, taking into account that positivity constraint on the original variable is transformed

https://doi.org/10.5194/egusphere-2026-5158
Preprint. Discussion started: 22 September 2026

Algorithm 1 Algorithm of the proposed Gibbs sampler.

Require: $\boldsymbol{M}, \boldsymbol{y}$, s (number of Gibbs samples), w (warm-up steps)
Ensure: Samples $\boldsymbol{x}^{(1)}, \boldsymbol{x}^{(2)}, \ldots, \boldsymbol{x}^{(s)}$ from the posterior distribution $p(\boldsymbol{x}|\boldsymbol{M}, \boldsymbol{y})$
Initialize: $\boldsymbol{x}^{(0)} \leftarrow \arg\min_{\boldsymbol{x} \geq \boldsymbol{0}} \|\boldsymbol{M}\boldsymbol{x} - \boldsymbol{y}\|_2^2$
Compute SVD: $\boldsymbol{M} = \boldsymbol{U}\boldsymbol{\Lambda}\boldsymbol{V}^\top$
Set $\boldsymbol{A} = \boldsymbol{U}\boldsymbol{\Lambda}$, $\boldsymbol{\alpha}^{(0)} = \boldsymbol{V}^\top \boldsymbol{x}^{(0)}$
for $m = 1$ to $s + w$ **do**
    Sample ω_y from Eq. (10)
    Sample ω_x from Eq. (9)
    for $i = 1$ to n **do**
        Sample $\alpha_i^{(m)}$ from Eq. (8)
    end for
    if $m \geq w + 1$ **then**
        $\boldsymbol{x}^{(m-w)} \leftarrow \boldsymbol{V}\boldsymbol{\alpha}^{(m)}$
    end if
end for

into different support of the transformed variable. In that case, the inequality changes sides and the corresponding bounds need to be adjusted. The minima and maxima of the possible solution have to be found by searching through all entries of vector $\boldsymbol{v}_i$.

4 Results

Below, we first quantify the annual posterior MPs emissions in the Western USA using the proposed model set-up, assuming spatiotemporal patterns weighted by the Gibbs sampling method (Section 3). This regional assessment helps both to evaluate the performance of the pattern-restricted inversion model in a regional domain and to establish a reference point for subsequent scaling to the global domain. We then extend the calculation over the global domain, a straightforward step given that the employed patterns are defined globally.

4.1 Estimated annual MPs emissions in the Western USA

The estimated posterior annual MPs emissions are given in Figure 1a for the inversion domain with the span of 124° to 91° W and 29° to 47° N. An annual total emission of 12.15 ± 8.45 million MPs particles per square meter were estimated in 5 different size bins, namely 5–10 μm, 10–25 μm, 25–50 μm, 50–100 μm, and 100–250 μm. The MPs size distribution has been measured in the dataset of Brahney et al. (2020) (see section 2.1). This annual total is half than the one reported by Evangeliou et al. (2022) for the same domain (22 ± 10 million particles $\mathrm{m}^{-2}\ \mathrm{y}^{-1}$). To calculate the emitted mass, we use the the average MPs density measured by Brahney et al. (2021) that is $\rho = 1.22$ g

https://doi.org/10.5194/egusphere-2026-5158
Preprint. Discussion started: 22 September 2026

cm^{-3}. According to their findings, 39% of the detected particles were spherical, while the rest (61%) were fragments (Brahney et al., 2021) exactly like those we simulated in the present study. Therefore, the conversion of number to mass emission of the particles is based on spheres (39%) and on cylinders (61%) considering the diameters measured by Brahney et al. (2021) as follows:

$$m_{sph} = \frac{4}{3}\pi\left(\frac{D_m}{2}\right)^3\rho, \tag{11}$$

for spheres, and

$$m_{cyl} = \frac{\pi}{4}A_{\text{ratio}}{D_m}^3\rho, \tag{12}$$

for cylinders,

where D_m and ρ are diameter and density measured by Brahney et al. (2020) and A_{ratio} is the aspect ratio for the modelled cylinders that represent fragments. The resulting total annual MP mass emissions from Eq. 11 and 12 were estimated to be 18.69 ± 13.10 Gg y^{-1} for the Western US domain. These emissions are 13 times smaller than those reported previously by the same group (Evangeliou et al., 2022: 244 ± 119 Gg y^{-1}).

Regarding the seasonal variability of the posterior MP emissions in the US (Figure 1a), the lowest emissions were found during summer months. Across most of the US, lower surface winds and reduced precipitation are most commonly observed in late summer to early autumn. During this period, the mid-latitude jet stream shifts northward and large-scale pressure gradients weaken, leading to fewer strong cyclones and more persistent high-pressure systems, which favor lighter winds and atmospheric stagnation. In the Western USA, particularly California and the Pacific Northwest, summer and early fall are climatologically dry due to the dominance of subtropical high pressure associated with the eastern Pacific High. Many interior regions also experience a relative precipitation minimum compared to the active spring storm season. While regional monsoons or tropical cyclones might occur in the Southeast, the summer period is broadly associated with weaker synoptic forcing, lower wind speeds, and reduced large-scale precipitation across the contiguous US (Marvel et al., 2023). These stagnant conditions cause lower resuspension of MPs and likely explain the observed annual minimum. In contrast, the seasonal MP emission maxima observed during spring and autumn agree with the wind-speed and precipitation maxima that are observed in most of the US during these seasons.

The comparison of measured with reconstructed modelled deposition rates for all size classes is shown in Figure 1b, while the different colors correspond to the respective size fractions of the posterior emissions. The reconstructed deposition rates have been calculated by coupling the calculated a posteriori emissions to the modelled SRMs. The calculated Pearson's correlation coefficient (r) for this case is 0.537, indicating a good linear relationship and thus a reasonably good reconstruction of the observed signal. Note that a good agreement between observations and reconstructed posterior deposition rates at this step does not justify any validation or methodological robustness. The reason for this is that the observed deposition rates shown in Figure 1b were used in the inverse algorithm and the latter has been designed to minimize the mismatch between posterior and observed deposition rates.

https://doi.org/10.5194/egusphere-2026-5158
Preprint. Discussion started: 22 September 2026

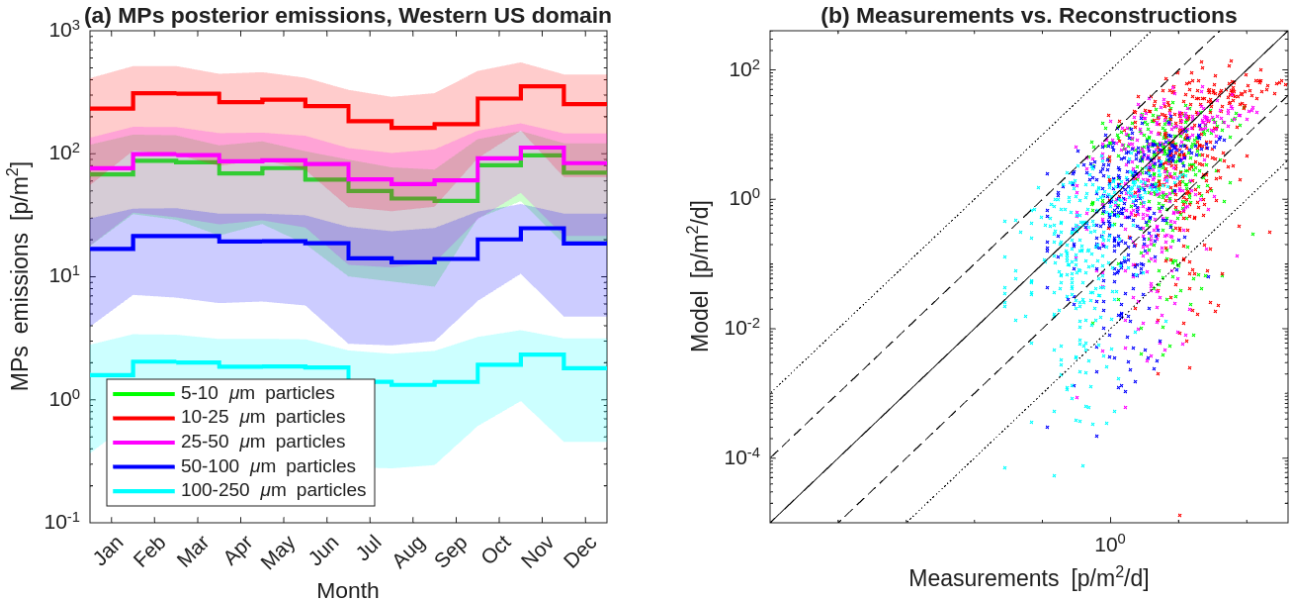

Figure 1. (a) Estimated posterior MPs emissions for the Western US domain (124° to 91° W and 29° to 47° N). Colors define the five different particle size classes (5-10 μm, 10-25 μm, 25-50 μm, 50-100 μm, 100-250 μm) and colored shades the associated uncertainty bounds defined here as one standard deviation of the posterior distribution. (b) Scatter-plot showing the fit between measured and modelled (reconstructed) deposition rates. The colors correspond to the same size classes that were plotted in Figure 1a.

4.2 Global atmospheric MPs emissions from continental and oceanic sources

The posterior emissions of atmospheric MP are inherently more reliable within the continental part of the Western USA, where they are constrained by the available measurements and their modelled SRMs. However, even a small oceanic coverage of the SRMs (<5% in our case, see Figure S4) can give an indication of the associated oceanic emissions that arrive at the receptors (national parks of the Western US, Brahney et al. (2021)). Nevertheless, more targeted measurements closer to the ocean would of course be more preferable, but the lack of robust analytical techniques for MP detection, accurate quantification, and source attribution hinder a comprehensive assessment of their distribution. Since the four patterns used for estimation in the West US domain are global, the posterior atmospheric MP emissions can be directly extrapolated over a global domain. The spatial accuracy of the posterior emissions now depends on the accuracy of each pattern. In the present study, the most updated data have been incorporated to build each pattern. Specifically, the most recent satellite-based land-cover maps have been processed to derive global agricultural emissions (Potapov et al., 2022). For bare soil resuspension, the FLEXDUST model (Groot Zwaaftink et al., 2017) was used together with the most recent assimilated data from ERA5, road dust was created using a bottom-up approach from IIASA's GAINS model (Evangeliou et al., 2020). Finally, the spatial

https://doi.org/10.5194/egusphere-2026-5158
Preprint. Discussion started: 22 September 2026

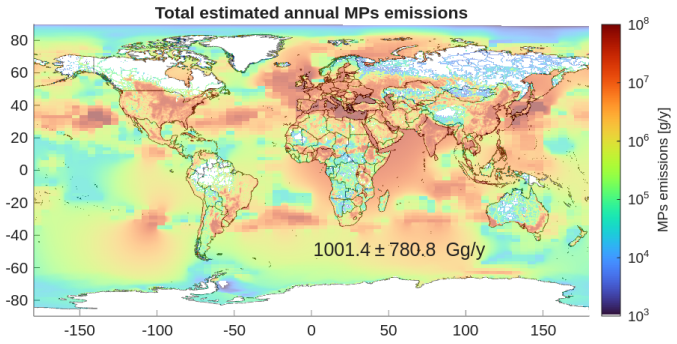

Figure 2. Spatial distribution of global annual posterior emissions of atmospheric MPs (1001 ± 781 Gg y^{-1}). The posterior emissions are the sum of the four different emission sectors that were assumed to contribute here, namely emissions from agricultural nets used in crop production, resuspension from bare soils, road dust, and ocean's surface. The calculated uncertainty is given as one standard deviation of the posterior distribution.

variability of the oceanic emissions of atmospheric MPs is based on gridded surface concentration data from Isobe et al. (2021) that were created from measurements conducted during 2000-2019 (see Section 3.2).

The spatial distribution of global atmospheric MP emissions from all continental and oceanic sources is shown in Figure 2. We estimate the annual atmospheric MPs emissions to be 1.46×10^{18} particles y^{-1}, which upon conversion to mass under our assumptions, becomes 1001 ± 781 Gg y^{-1}. This is a substantially lower estimate compared to previous estimates using the same data. For instance, they are almost 9 times lower than the annual global emissions of 8700 Gg y^{-1} reported by Brahney et al. (2021) and one order of magnitude lower than 9600 ± 3600 Gg y^{-1} reported by Evangeliou et al. (2022) using a similar inverse modelling approach, but considering only spherical particles in the model. The spatial distribution of the annual global emissions of atmospheric MPs from agricultural, road, bare soil and oceanic sectors are depicted in Figure 3. Their uncertainty bounds have been derived from the Gibbs sampler (Figure S4). The largest contributor is the oceanic sector that releases 1.11×10^{18} particles y^{-1} or 763 ± 611 Gg y^{-1} for 5-250 μm. This is consistent with previously estimates reporting that the large oceanic surface, the final receptor of larger plastics, has accumulated several tons of plastics (4800 to 12700 Gg y^{-1}, Jambeck et al. (2015)), that can be remobilised as a result of bubble bursting and wave breaking into the shore releasing plastic debris back to the atmosphere (Allen et al., 2020; Fu et al., 2023). However, the relative importance of oceanic contribution is smaller in our study. While Brahney et al. (2021) and Evangeliou et al. (2022) attributed 98.9% and 92.7%, respectively, to oceanic MPs emissions with respect to the total annual emissions, our current estimate suggests a maximum contribution of 76.8%. This indicates a relatively stronger contribution from continental sources in our framework.

The spatial distribution of the total annual MP emissions among the four considered sectors is depicted in Figure 3. The detailed contribution to annual MP emissions from each sector (agricultural nets, bare soils, road dust and oceanic emissions) can be seen in Table 1. Except for the oceanic emissions, agricultural emissions add 2.7×10^{17}

https://doi.org/10.5194/egusphere-2026-5158
Preprint. Discussion started: 22 September 2026

particles y^{-1} or 170 ± 124 Gg y^{-1}, upon conversion to mass for sizes for 5-250 μm, road dust gives another 7.5×10^{16} particles y^{-1} or 51 ± 31 Gg y^{-1}, and bare soils 2.6×10^{16} particles y^{-1} or 17 ± 14 Gg y^{-1}. Regions expected to exhibit the highest agricultural MP emissions largely coincide with the world's most intensively cultivated croplands. These include the Indo-Gangetic Plain (India–Pakistan–Bangladesh), one of the most productive and intensively managed agricultural systems globally, dominated by rice–wheat rotations and high cropping intensity (Pingali, 2012; Lobell et al., 2011). The US Midwest (Iowa, Illinois, Indiana, Nebraska, Minnesota) represents one of the largest contiguous high-yield maize-soybean production regions worldwide (Ray et al., 2013). Similarly, the North China Plain is characterized by intensive wheat-maize double-cropping systems and high fertilizer and irrigation inputs (Su et al., 2021). In addition, Europe and the Eurasian steppe region (Ukraine–Russia–Kazakhstan) constitutes a major global wheat and barley production belt with extensive cultivated land area (Ray et al., 2012). These regions collectively account for a substantial fraction of global harvested cropland and agricultural production, and are therefore likely hotspots of agricultural emissions of MPs (Figure 3). Regarding resuspended MPs from bare soils, West Asia and North Africa are the most significant regions, while resuspension from Europe, Russia, and Oceania is much smaller due to the smaller mineral dust emissions in these regions. Finally, MPs emissions from bare soils are particularly high in the Middle East, where both population density and mineral dust emissions are high (Evangelou et al., 2024). Road dust emissions agree well with the distribution of global population and are more significant in the west coast of the US, Europe and Southeastern Asia (Figure 3). Finally, oceanic hotspot emissions of MPs coincide with the locations of the garbage patches, exactly as in Isobe et al. (2021) dataset that was used to scale emissions globally. A recent study showed that a storm event at the great garbage patch of the North Atlantic ocean caused intensive deposition of the order of 113,000 particles m^{-2} d^{-1}, with pre- and post- event deposition was only 700 and 30,000 particles m^{-2} d^{-1}, respectively (Ryan et al., 2023). This shows that the oceanic garbage patches are likely a significant source of atmospheric MPs.

The region-specific contributions to annual global atmospheric MP emissions are summarized in Table 2, based on the geographical definition presented in Figure 4a. Considering particle size bins spanning 5–250μm, Asia emerges as the dominant source region, with an estimated annual emission of 1.35×10^{17} particles y^{-1}, corresponding to 88 ± 62 Gg y^{-1} when expressed in mass units. Asia's leading contribution reflects not only its large geographical extent, but also its high population density, intensive agricultural practices, extensive urbanization, and industrial activity. These factors enhance primary emissions and resuspension favoring elevated atmospheric MP fluxes. In particular, densely populated and agriculturally intensive regions, such as the Indo-Gangetic Plain and eastern China, are likely to act as regional hotspots. The American continent (including North, Central, and South America) constitutes the second-largest emitting region, contributing approximately 9.3×10^{16} particles y^{-1} or 60 ± 42 Gg y^{-1}. Within this aggregate, North America accounts for the majority of emissions (Table 2), reflecting extensive agricultural activity, large urbanized areas, and significant road networks that enhance both direct emissions and resuspension. South and Central America contribute comparatively less, although expanding agricultural practices and land-use change may locally intensify emissions. Europe contributes 4.3×10^{16} particles y^{-1}, corresponding to 28 ± 20 Gg y^{-1}. Emissions in

https://doi.org/10.5194/egusphere-2026-5158
Preprint. Discussion started: 22 September 2026

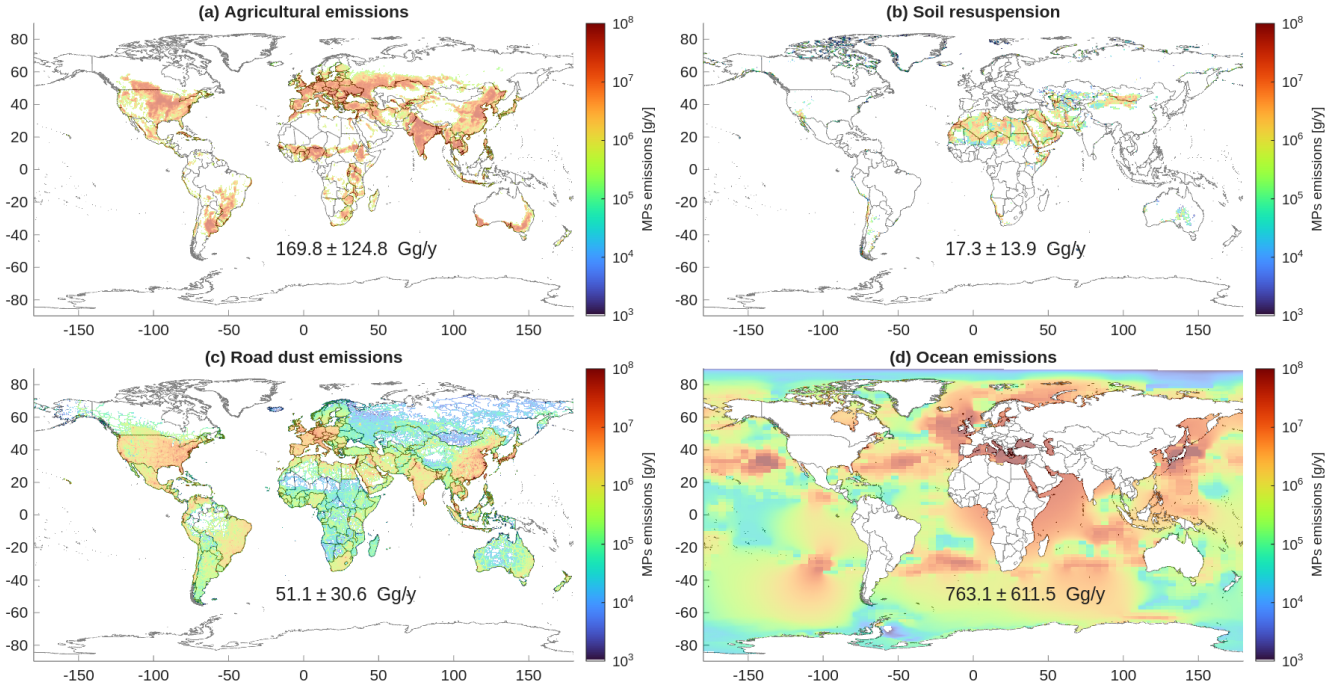

Figure 3. Spatial distribution of global annual posterior emissions of atmospheric MPs for the four different emission sectors. Emissions from agricultural nets used in crop production contribute a total 170 ± 125 Gg y^{-1}, bare soils only 17 ± 14 Gg y^{-1}, road dust contribute 51 ± 31 Gg y^{-1}, and oceanic emissions 763 ± 611 Gg y^{-1}. The calculated uncertainty for each sector is given as one standard deviation of the posterior distribution.

Europe are closely linked to intensive agriculture, dense transportation infrastructure, and high levels of urbanization. Notably, Russia, spanning both Europe and Asia, accounts for an additional 2.3×10^{16} particles y^{-1} (15 ± 11 Gg y^{-1}). Although Russia's population density is lower than that of Western Europe, its vast land area and extensive agricultural zones contribute substantially to its overall MP emissions. Africa emits approximately 5.2×10^{16} particles y^{-1}, or 34 ± 25 Gg y^{-1}. In contrast to other regions, a considerable fraction of African emissions is associated with bare soil resuspension processes rather than intensive industrial or agricultural sources. The existence of arid and semi-arid ecosystems, combined with strong wind-driven dust mobilization, enhances the potential for atmospheric entrainment of MPs present in soils. Oceania contributes a comparatively minor share, with 1.2×10^{16} particles y^{-1} or 7.4 ± 5.4 Gg y^{-1}. Despite its large geographical area, the region's relatively low population density and lower intensity of anthropogenic activities result in reduced MP emissions. Furthermore, total dust emissions are lower compared to other continents, limiting the contribution from resuspension-driven pathways. Overall, the regional distribution of atmospheric MP emissions reflects a combined influence of population density, land use, agricultural intensity, and soil resuspension potential. Regions characterized by dense human activity and intensive land management tend to

https://doi.org/10.5194/egusphere-2026-5158
Preprint. Discussion started: 22 September 2026

Table 1. Contribution of the four considered emission sectors (agricultural nets in croplands, bare soil resuspension, road dust and surface oceanic) to annual global atmospheric MPs emissions.
⋆ particles 5–70 μm; ⋆⋆ particles 5–100 μm; ⋆⋆⋆ particles 5–250 μm; † MMPW (mismanaged plastic waste) in (Fu et al., 2023) assigned here to the soil resuspension category for comparison only.

MPs [Gg/y and p/y]	Agriculture	Soil resusp.	Road dust	Ocean
Brahney et al. (2021)⋆⋆	18	68	96	8600
	7.1×10^{16}	2.7×10^{17}	3.8×10^{17}	3.39×10^{19}
Evangeliou et al. (2022)⋆⋆⋆	310 ± 130	100 ± 52	280 ± 120	9600 ± 3600
	2.52×10^{18}	8.1×10^{17}	2.27×10^{18}	7.80×10^{19}
Fu et al. (2023)⋆	37.3	0.11†	114.4	169.8
	6.7×10^{17}	2.0×10^{15}	2.1×10^{18}	3.1×10^{18}
Yang et al. (2025)⋆	5000	300	5000	0.8
	4.9×10^{18}	2.9×10^{17}	4.9×10^{18}	7.8×10^{14}
Evangelou et al. (2026) (spheres)⋆⋆	0.5			4.6
	6.07×10^{17}			2.7×10^{16}
Evangelou et al. (2026) (sph+cyl)⋆⋆	12.5			104.77
	6.07×10^{17}			2.7×10^{16}
this study⋆⋆⋆	169.8 ± 124.8	17.3 ± 13.9	51.1 ± 30.6	763 ± 611
	2.7×10^{17}	2.6×10^{16}	7.5×10^{16}	1.1×10^{18}

dominate mass and particle fluxes, whereas sparsely populated regions contribute primarily through resuspension. The substantial uncertainties associated with all regions (typically exceeding 50% relative uncertainty) highlight the need for improved constraints on emission factors, land-surface MP reservoirs, and resuspension dynamics.

The size-resolved annual global MP emission inventory reveals a pronounced dependence of both mass and particle number fluxes on particle diameter. Emissions were quantified for five size classes spanning 5–250 μm, expressed in terms of annual mass flux (Gg y^{-1}) and corresponding particle number flux (particles y^{-1}) in Table 3. In the smallest size fraction (5–10 μm), total emissions amount to 1.4 ± 1.0 Gg y^{-1}, corresponding to approximately 2.2×10^{17} particles y^{-1}. Although this bin contributes only a minor fraction of the total emitted mass, it accounts for a substantial number of particles, reflecting the strong inverse scaling between particle size and particle number. The 10–25 μm size class shows a marked increase in mass flux, reaching 56 ± 43 Gg y^{-1}, with a corresponding number flux of 8.7×10^{17} particles y^{-1}. This size range represents the largest particle number contribution across all

https://doi.org/10.5194/egusphere-2026-5158
Preprint. Discussion started: 22 September 2026

Table 2. Continental contribution to annual global atmospheric MPs emissions from the regions defined in Figure 4a.
⋆ particles 5–70 μm; ⋆⋆ particles 5–100 μm; ⋆⋆⋆ particles 5–250 μm

MPs [Gg/y and p/y]	Asia	Russia	Greenland	Europe	N. Amer.	C. Amer.	S. Amer.	Africa	Oceania	Antarctica	Ocean	Total
Brahney et al. (2021) ⋆⋆	88	2.3	0.012	49	24	3.1	7.1	9.3	3.9	9.8×10^{-5}	8600	8700
	3.4×10^{17}	9.0×10^{15}	4.7×10^{13}	1.9×10^{17}	9.4×10^{16}	1.2×10^{16}	2.8×10^{16}	3.6×10^{16}	1.5×10^{16}	3.8×10^{11}	3.4×10^{19}	3.4×10^{19}
Evangeliou et al. (2022) ⋆⋆⋆	250 ± 120	44 ± 20	18 ± 95	88 ± 42	130 ± 55	15 ± 7.8	45 ± 22	110 ± 55	12 ± 5.8	0.09 ± 0.046	8900 ± 3500	9600 ± 3600
	2.0×10^{18}	3.5×10^{17}	1.4×10^{17}	7.0×10^{17}	1.0×10^{18}	1.2×10^{17}	3.6×10^{17}	8.8×10^{17}	9.6×10^{16}	7.2×10^{14}	7.1×10^{19}	7.6×10^{19}
this study⋆⋆⋆	87.8 ± 62.3	14.6 ± 10.7	0.004 ± 0.003	27.9 ± 19.7	40.7 ± 28.3	3.4 ± 2.3	16.1 ± 11.3	33.8 ± 25.0	7.4 ± 5.4	0 ± 0	763.1 ± 611.5	1001.5 ± 780.9
	1.35×10^{17}	2.29×10^{16}	6.56×10^{12}	4.33×10^{16}	6.28×10^{16}	5.21×10^{15}	2.49×10^{16}	5.21×10^{16}	1.16×10^{16}	0	1.11×10^{18}	1.47×10^{18}
Fu et al. (2023) ⋆	57.5	3.2	0.0	3.8	15.2	8.4	15.7	23.9	9.2	0.0	185.5	322.5
	1.0×10^{18}	5.7×10^{16}	1.9×10^{11}	6.9×10^{16}	2.7×10^{17}	1.5×10^{17}	2.8×10^{17}	4.3×10^{17}	1.7×10^{17}	8.0×10^{7}	3.3×10^{18}	5.8×10^{18}
Yang et al. (2025) ⋆	3647.2	589.9	0.2	1511.0	2154.3	170.9	661.3	942.9	254.2	0	396.9	10328.8
	3.5×10^{18}	5.7×10^{17}	1.7×10^{14}	1.5×10^{18}	2.1×10^{18}	1.7×10^{17}	6.4×10^{17}	9.2×10^{17}	2.5×10^{17}	0	3.9×10^{17}	1.0×10^{19}
Evangelou et al. (2026) (sph) ⋆⋆	0.214	0.039	6.4×10^{-6}	0.075	0.096	0.025	0.047	0.051	0.091	9.4×10^{-12}	4.6	5.155
	1.8×10^{17}	4.2×10^{16}	3.7×10^{10}	8.2×10^{16}	1.0×10^{17}	2.6×10^{16}	5.0×10^{16}	4.8×10^{16}	1.2×10^{16}	5.4×10^{4}	2.7×10^{16}	6.3×10^{17}
Evangelou et al. (2026) (sph+cyl) ⋆⋆	4.87	0.89	0.0002	1.71	2.19	0.58	1.07	1.17	2.09	2.2×10^{-10}	104.77	117.27
	1.8×10^{17}	4.2×10^{16}	3.7×10^{10}	8.2×10^{16}	1.0×10^{17}	2.6×10^{16}	5.0×10^{16}	4.8×10^{16}	1.2×10^{16}	5.4×10^{4}	2.7×10^{16}	6.3×10^{17}
this study ⋆⋆	51.6 ± 36.5	8.6 ± 6.3	0.003 ± 0.002	16.4 ± 11.6	23.9 ± 16.6	2.0 ± 1.4	9.5 ± 6.6	19.9 ± 14.7	4.4 ± 3.2	0 ± 0	443.3 ± 354.8	583.4 ± 454.2
	1.34×10^{17}	2.28×10^{16}	6.53×10^{12}	4.31×10^{16}	6.25×10^{16}	5.18×10^{15}	2.47×10^{16}	5.19×10^{16}	1.15×10^{16}	0	1.10×10^{18}	1.46×10^{18}

https://doi.org/10.5194/egusphere-2026-5158
Preprint. Discussion started: 22 September 2026

bins, suggesting that intermediate-sized MPs dominate the total emitted particle abundance despite not contributing the highest mass. For the 25–50 μm fraction, emissions further increase in mass to 187 ± 146 Gg y^{-1}, while the particle number decreases to 3.0×10^{17} particles y^{-1}. This shift reflects the cubic dependence of particle mass on diameter, whereby increasing particle size disproportionately enhances mass contributions relative to particle counts. The 50–100 μm class contributes 339 ± 264 Gg y^{-1}, accompanied by 6.7×10^{16} particles y^{-1}. Despite a continued increase in mass flux, the number flux decreases by approximately one order of magnitude compared to the 10–25 μm class. The largest size fraction (100–250 μm) exhibits the highest mass contribution, 418 ± 327 Gg y^{-1}, yet the lowest particle number flux, approximately 6.5×10^{15} particles y^{-1}. This size class therefore dominates total emitted mass but contributes minimally to the total particle abundance.

Table 3. Contribution of the examined size-fractions to the annual global atmospheric MPs emissions.
⋆ particles 5–70 μm; ⋆⋆ particles 5–100 μm; ⋆⋆⋆ particles 5–250 μm

MPs[Gg/y and p/y]	5–10 μm	10–25 μm	25–50 μm	50–100 μm	100–250 μm
Brahney et al. (2021)⋆⋆	62	140	1100	7400	–
	2.4×10^{19}	3.6×10^{18}	3.9×10^{18}	2.8×10^{18}	–
Evangeliou et al. (2022)⋆⋆⋆	7.9 ± 3.1	110 ± 50	500 ± 230	2000 ± 920	7300 ± 3000
	2.4×10^{19}	3.2×10^{19}	1.5×10^{19}	7.4×10^{18}	2.1×10^{18}
Fu et al. (2023)⋆	0.65	0.65	0.65	320.6	–
	3.6×10^{18}	3.7×10^{17}	2.9×10^{16}	1.8×10^{18}	–
Yang et al. (2025)⋆	136.9	1121.1	3202.5	5868.3	–
	4.8×10^{18}	4.9×10^{18}	3.3×10^{17}	7.4×10^{16}	–
Evangelou et al. (2026) (spheres)⋆⋆	0.12	0.16	0.31	4.56	–
	5.4×10^{17}	6.6×10^{16}	1.1×10^{16}	2.1×10^{16}	–
Evangelou et al. (2026) (sph+cyl)⋆⋆	2.71	3.72	7.07	103.78	–
	5.4×10^{17}	6.6×10^{16}	1.1×10^{16}	2.1×10^{16}	–
this study⋆⋆⋆	1.4 ± 1.0	55.9 ± 43.4	187.3 ± 145.8	338.8 ± 263.9	418.1 ± 326.7
	2.2×10^{17}	8.7×10^{17}	3.0×10^{17}	6.7×10^{16}	6.5×10^{15}

4.3 Independent validation of global emissions

In this section, we assess the robustness of our global emission estimates. While the reconstructed concentrations and deposition rates provide a basis to show the performance of the inversion (Figure 1b), they cannot be considered

https://doi.org/10.5194/egusphere-2026-5158
Preprint. Discussion started: 22 September 2026

a sufficient validation, because the inversion has been designed to reduce the model-observation mismatches. The magnitude of the posterior reduction of the model mismatch to the observations is partly determined by the weighting given to the observations relative to the prior emissions. A robust validation can only be performed via comparison of the posterior concentrations with observations that were not included in the inversion (independent observations). For this, a public global measurement dataset was adopted from Evangelou et al. (2026) presenting concentrations and deposition rates of atmospheric MPs gathered from the literature during the last 10 years. The posterior emissions presented in this study were coupled with modelled SRMs for the independent measurements and the calculated posterior modelled concentrations were compared with the observations (Figure 4b).

To match modelled size fractions with the measured fibers and fragments, the volume equivalent diameter d_{eq} was calculated assuming cylinders with the average length L and width d of the reported particles. If the width was not reported, an aspect ratio (L/d) of 40 and 2 was used for fibers and fragments, respectively. For spherical particles, the reported size was used as d_{eq}. Films were represented as square-shaped particles with a thickness S of 5 μm and a diagonal dimension L equal to the average measured size. For fibers and fragments, the volume is

$$V = \pi \left(\frac{d}{2}\right)^2 L \text{ whereas, for films } V = \pi \left(\frac{S}{2}\right)^2 L \tag{13}$$

and,

$$d_{\mathrm{eq}} = 2\left(\frac{3V}{4\pi}\right)^{1/3} \tag{14}$$

Except for the posterior emissions from this study, we performed the same calculations using public emission datasets from Fu et al. (2023), Yang et al. (2025) and Evangelou et al. (2026) (Figure 4c-f). Fu et al. (2023) reported gridded MP emissions for different size fractions of 0.3–70 μm. Similarly, Yang et al. (2025) reported (non-gridded) annual mass emissions per size fraction (< 70 μm). They assumed that the major MP sources would be continental emissions (10,000 Gg/y) with a relatively insignificant source from the ocean (0.8 Gg/y) and bare soil resuspension of 300 Gg/y. To get the spatial distribution of their emissions, we split the continental sources equally into agricultural and road dust emissions (5,000 Gg/y each) and used the same patterns as those used here (Figure S2) to distribute these masses in a global domain. To further convert from mass to number emissions, we assumed particles to be cylinders with aspect ratio of 20 (resulting into posterior emissions that were used in Figure 4d) and spheres (used in Figure 4e), both with same density as the one measured by Brahney et al. (2020) ($\rho = 1.22$ g cm^{-3}). Finally, MP emissions from Evangelou et al. (2026) for continental and oceanic sources were also included in the comparison. The scatterplots of the comparisons are illustrated in Figure 4.

The performance of each emission inventory was assessed using the coefficient of determination evaluated in logarithmic space for modelled and measured MPs, $R^2_{\log_{10}}$, defined as:

$$R^2_{\log_{10}} = 1 - \frac{\sum_{i=1}^{p} \left(\log_{10} y_i - \log_{10} \hat{y}_i\right)^2}{\sum_{i=1}^{p} \left(\log_{10} y_i - \overline{\log_{10} y}\right)^2}, \tag{15}$$

https://doi.org/10.5194/egusphere-2026-5158
Preprint. Discussion started: 22 September 2026

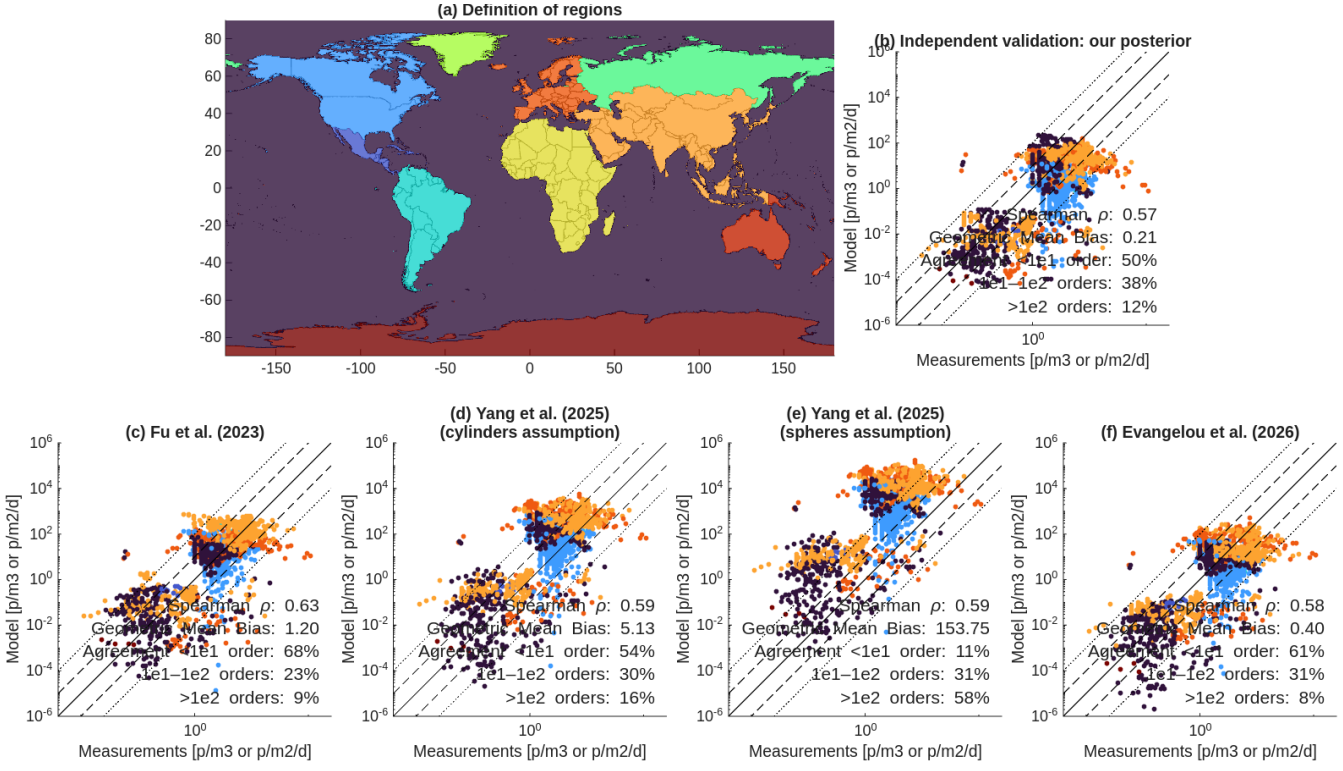

Figure 4. (a) Region definition to show different locations of measurements. (b) Posterior modelled concentrations and deposition rates against independent observations using emissions from this study. (c) Modelled concentrations and deposition rates against independent observations using emissions from (Fu et al., 2023), using emissions from Yang et al. (2025) assuming (d) cylindrical and (e) spherical shape, and (f) modelled concentrations and deposition rates against independent observations using emissions from Evangelou et al. (2026).

where y_i are the observed values, $\hat{y}_i$ are the modeled values, $\overline{\log_{10} y}$ denotes the mean of the logarithm of observations, and p is the number of observations. In addition, the geometric mean bias (GMB) was used defined as:

$$\mathrm{GMB} = 10^{\frac{1}{p}\sum_{i=1}^{p}\log_{10}\left(\frac{\hat{y}_i}{y_i}\right)}, \tag{16}$$

where $\hat{y}_i$ and y_i are the modeled and observed values, respectively. A value of GMB close to unity indicates no systematic bias, values larger indicate overestimation, and values smaller than unity indicate underestimation. Finally, Spearman rank correlation coefficient, ρ, was used defined as:

$$\rho = \frac{\mathrm{cov}\,(R_x, R_y)}{\sigma_{R_x}\sigma_{R_y}} = 1 - \frac{6\sum_{i=1}^{p} d_i^2}{p\,(p^2-1)}, \tag{17}$$

where R_x is the rank variable, σ_{R_x} is its standard deviation, $d_i = R_x - R_y$ is the difference between the two ranks of each observation, and p is the number of observations.

https://doi.org/10.5194/egusphere-2026-5158
Preprint. Discussion started: 22 September 2026

Figure 4 shows that our posterior emissions captured the broad variability of the measurements and reproduced the main gradients in both atmospheric concentrations and deposition. The Spearman correlation coefficient of 0.57 indicates a reasonably strong monotonic relationship between the observations and the modelled values, suggesting that our modelling framework is able to represent the large-scale spatiotemporal patterns of atmospheric MPs at the global scale. The calculated GMB for our posterior simulation (0.21) shows underestimation of the observations, so as Evangelou et al. (2026) (0.40). In contrast, the posterior emissions from Yang et al. (2025), for both cylindrical and spherical particle shapes, produce systematically overestimated modelled values, with GMBs of 5.1 and 153.75, respectively, so as Fu et al. (2023) emissions do (GMB=120).

Using our posterior emissions, 50% of the modelled concentration and deposition rates fall within one order of magnitude from the observations, 88% fall within two orders of magnitude, and only 12% can be considered clear outliers. Similar statistics were obtained using the emissions from Fu et al. (2023) (68% - 91% - 9%) and Evangelou et al. (2026) (61% - 92% - 8%), whereas Yang et al. (2025) emissions lead to a substantially larger fraction of modelled values lying more than two orders of magnitude away from the observations (16% when cylinders and 58% when spheres were assumed). Overall, these results show that our posterior emissions provide a more balanced agreement with the available measurements, without the strong positive bias seen in the other reported inventories. Overall, the validation supports our conclusion that the current inversion framework is able to provide a realistic emission inventory for atmospheric MPs, even though notable discrepancies remain at individual sites and for specific samples.

4.4 Estimated posterior uncertainty

Uncertainties in the posterior MPs emissions were quantified using two complementary approaches, capturing both the statistical variability of the posterior distribution and the sensitivity to atmospheric transport modeling. Firstly, we quantify the uncertainty of the posterior MPs emissions directly from the samples generated by the Gibbs sampler (see Section 3.3). The Gibbs sampling algorithm provides a sequence of samples $\{\boldsymbol{x}^{(s)}\}_{s=1}^{S}$ drawn from the posterior distribution $p(\boldsymbol{x} \mid \boldsymbol{y}, \boldsymbol{M})$, thereby providing a fully probabilistic characterization of the solution. This Gibbs-based approach is beneficial, because it does not only yield a single optimal estimate, but also characterizes the spread of plausible emission fields consistent with the observations, the prior assumptions, and the forward model. For each emission element x_i, corresponding to each grid-cell, we estimate the posterior mean and standard deviation from the samples as

$$\mu_{x_i} = \frac{1}{S}\sum_{s=1}^{S} x_i^{(s)}, \tag{18}$$

$$\sigma_{x_i} = \sqrt{\frac{1}{S-1}\sum_{s=1}^{S}\left(x_i^{(s)} - \bar{x}_i\right)^2}, \tag{19}$$

https://doi.org/10.5194/egusphere-2026-5158
Preprint. Discussion started: 22 September 2026

where μ_{x_i} represents the posterior expectation and σ_{x_i} quantifies the associated uncertainty. This uncertainty reflects the combined effects of observational noise, model representation errors, and prior constraints, as encoded in the posterior distribution.

Secondly, we assessed the sensitivity of the posterior emissions to uncertainties in the atmospheric transport parameterizations, with particular emphasis on wet scavenging. This step is important because wet deposition is one of the main removal pathways for MPs from the atmosphere, and changes in scavenging efficiency directly affect lifetime, transport distance, and the SRMs used to reproduce the observations. Stronger scavenging removes particles more efficiently during transport, which tends to reduce long-range transport and can shift the inversion toward larger or more localized source estimates. On the contrary, weaker scavenging allows particles to remain in the atmosphere longer, enhances transport away from source regions leading to different posterior emission patterns. To quantify this sensitivity, we repeated the inversion using atmospheric simulations with different CCN/IN efficiencies, corresponding to low, medium, and high scavenging scenarios (see Section 2.2 for details). Each of these scenarios defines a different transport-removal regime and therefore yields a different posterior emission estimate. The standard deviation of the posterior emissions across the different inversions was used as a measure of the uncertainty associated with the representation of wet deposition in the model. This aspect is particularly crucial in the present study because scavenging coefficients for MPs have never been measured directly, and the adopted parameters that are currently used in FLEXPART are not observationally constrained and remain an important source of model uncertainty.

Together, these two approaches allow us to distinguish between uncertainty arising from the inversion framework itself and uncertainty related to atmospheric process representation. The results are shown in Figure 5, where both panels are displayed on a logarithmic scale. The contrast between the two estimates is clear. In Figure 5(a), the uncertainty derived from Gibbs sampling is spatially widespread and large, with elevated values over most major continental regions, such as North America, Europe, Africa, and Asia. Much of the calculated uncertainty falls within the range of about 10^{-3} to 10^{-1} Gg y^{-1}, especially in regions where the posterior emissions are substantial. In contrast, Figure 5(b) shows that the uncertainty associated with scavenging is generally much smaller and more spatially muted. Most of the domain is characterized by values between about 10^{-5} and 10^{-3} Gg y^{-1}, with only localized regions showing somewhat larger response to the different scavenging coefficients. The uncertainty associated with scavenging parameterization is negligible compared to the posterior uncertainty estimated from the Gibbs sampler.

Overall, the two uncertainty estimates differ by roughly one to two orders of magnitude over large parts of the globe. This demonstrates that the total uncertainty in the inferred MPs emissions is dominated by the statistical variability of the Gibbs inversion, while the additional uncertainty introduced by the scavenging parameterizations is tiny. In other words, within the range of low-, medium-, and high-scavenging scenarios considered here, the posterior solution appears to be much more strongly affected by the internal spread of the Bayesian inversion than by the specific choice of scavenging efficiency. Our findings suggest that, although wet deposition remains an important and

https://doi.org/10.5194/egusphere-2026-5158
Preprint. Discussion started: 22 September 2026

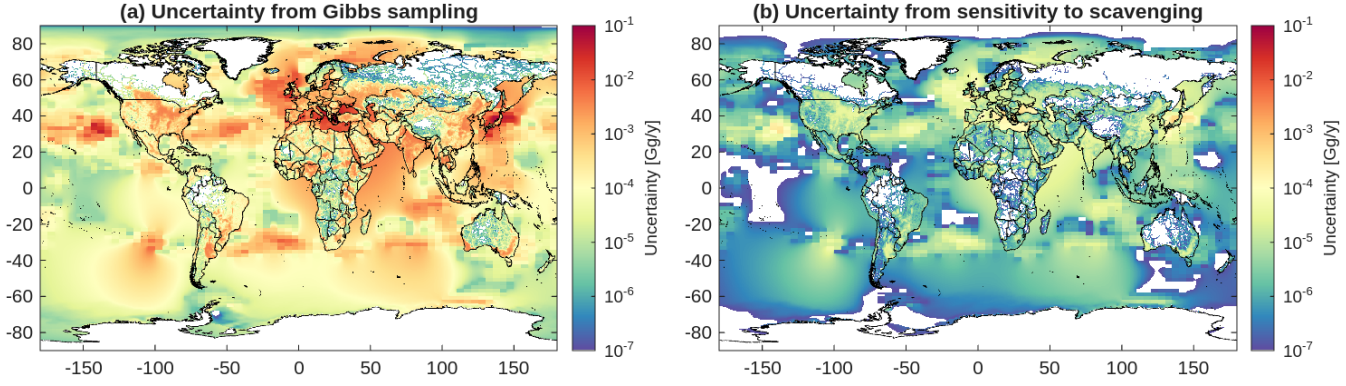

Figure 5. Uncertainty of posterior MPs emissions derived from (a) Gibbs sampling and (b) sensitivity to scavenging parameterizations. Both panels are shown on a logarithmic scale.

unconstrained process for MPs, its contribution to the posterior emission uncertainty is secondary compared with the uncertainty represented by the posterior distribution itself.

5 Discussion

5.1 Comparison with previously-reported bottom-up and top-down global estimates

During the last five years, atmospheric measurements of MPs in air and deposition have expanded rapidly leading to a first generation bottom-up and top-down estimates of their emissions to the atmosphere (see Table 1). The comparison between our posterior MP emissions and literature emissions illustrate that the global atmospheric MP budget remains highly uncertain (Table 1). Depending on the study and the sector, reported annual emissions span very broad ranges, from tens to thousands of Gg y^{-1} for agriculture, from less than 1 to several hundred Gg y^{-1} for soil resuspension, from about 50 to 5000 Gg y^{-1} for road dust, and from less than 1 to nearly 10,000 Gg y^{-1} for the oceanic source. Similar variability is found in particle-number estimates, which range from about 10^{15} to 10^{20} particles y^{-1}. This wide spread highlights the strong sensitivity of global emissions to the selected analytical methodologies used to define environmental levels, the measured size distributions and the assumed densities and shapes that lead to different conversions between particle numbers and masses.

Our posterior estimates define a more moderate but still ocean-dominated global budget. We report emissions of 170 ± 125 Gg y^{-1} from agriculture, 17 ± 14 Gg y^{-1} from soil resuspension, 51 ± 31 Gg y^{-1} from road dust, and 763 ± 611 Gg y^{-1} from the surface ocean. In partical terms, these correspond to approximately 2.7×10^{17}, 2.6×10^{16}, 7.6×10^{16}, and 1.1×10^{18} particles y^{-1}, respectively. The resulting total emission is therefore 1001 Gg y^{-1}, or about 1.5×10^{18} particles y^{-1}. This total is substantially lower than the large global emissions reported by Brahney et al.

https://doi.org/10.5194/egusphere-2026-5158
Preprint. Discussion started: 22 September 2026

(2021), Evangeliou et al. (2022) and Yang et al. (2025), but higher than the more conservative estimate of Fu et al. (2023) and Evangelou et al. (2026).

The sectoral partitioning obtained here is also very informative. In our estimate, the ocean remains the dominant source, contributing roughly three quarters of the total mass and particle number, but its role is less extreme than in studies where marine emissions exceed 90% of the global total (see also next section). Our oceanic estimate is markedly lower than the very large oceanic values proposed by Brahney et al. (2021) and Evangeliou et al. (2022), suggesting that the importance of the ocean remains one of the major unresolved issues in the global atmospheric MP cycle. Agriculture emerges as the second most important sector, whereas soil resuspension and road dust have smaller shares. This differs from studies that emphasize much stronger traffic-related or dust-driven emissions, and especially from Yang et al. (2025), where terrestrial sources dominate and oceanic emissions are almost negligible.

Table 1 further shows that part of the disagreement between studies does not arise solely from differences in source strength, but also from how MPs are physically represented. This is particularly evident in Evangelou et al. (2026) estimates, who represented MPs as films, fragments and spheres in their model, but assumed spherical particle shapes when converting from number emissions leading to large differences in mass emissions from our posterior, even though particle number emissions remain of the same order of magnitude. Such differences underline that comparisons between studies must be made with caution, because contrasting budgets may reflect not only different emission processes, but also different assumptions regarding particle geometry, size distributions, and density. Overall, our results fall well within the range of recent published values, while supporting a preliminary interpretation of the global atmospheric MP budget, neither marine- nor dust-dominated, but rather a mixed system in which oceanic emissions remain the largest contributor and terrestrial sources, particularly agriculture and road dust, hold a substantial share.

At the regional scale (see region definition in Figure 4a), the estimates compiled in Table 2 show that our spatial distribution of atmospheric MP emissions is overall much closer to the lower or intermediate range of the literature than to the highest regional budgets published so far. As shown already, the ocean remains the dominant source region, with 763 ± 611 Gg y^{-1} (out of a global total of 1001 ± 781 Gg y^{-1}). Thus, roughly three quarters of the global atmospheric MP budget in our framework is of marine origin, while all land regions combined contribute about 238 Gg y^{-1}. Within the continental domain, the largest source is Asia (88 ± 62 Gg y^{-1}), followed by North America (41 ± 28 Gg y^{-1}), Africa (34 ± 25 Gg y^{-1}), Europe (28 ± 20 Gg y^{-1}), South America (16 ± 11 Gg y^{-1}), Russia (15 ± 11 Gg y^{-1}), Oceania (7.4 ± 5.4 Gg y^{-1}), Central America (3.4 ± 2.3 Gg y^{-1}), Greenland (0.004 ± 0.003 Gg y^{-1}), and Antarctica (0 Gg y^{-1}). This ranking indicates that Asia alone contributes nearly 38% of the total land emissions, while Asia, North America, and Africa together account for about 70% of the continental budget. The same geographical structure is reproduced in particle number emissions, with 1.1×10^{18} emitted from the ocean out of a global total of 1.47×10^{18} particles y^{-1}, confirming that the dominance of the ocean globally and of Asia, North America, Africa, and Europe among land regions is robust in both mass and number terms.

https://doi.org/10.5194/egusphere-2026-5158
Preprint. Discussion started: 22 September 2026

Compared with Brahney et al. (2021), our estimates are similar in some key regions, especially Asia, where our value (88 ± 62 Gg y^{-1}) is identical to their, and Central America, where our estimate of 3.4 ± 2.3 Gg y^{-1} is very close to their 3.1 Gg y^{-1}. For Greenland, both studies also indicate only a negligible contribution, although our value (0.004 ± 0.003 Gg y^{-1}) is lower than the 0.012 Gg y^{-1} reported by Brahney et al. (2021). In several other continental regions, however, our estimates are higher than those of Brahney et al. (2021), including Russia (15 ± 11 vs 2.3 Gg y^{-1}), North America (41 ± 28 vs 24 Gg y^{-1}), South America (16 ± 11 vs 7.1 Gg y^{-1}), Africa (34 ± 25 vs 9.3 Gg y^{-1}), and Oceania (7.4 ± 5.4 vs 3.9 Gg y^{-1}). Europe is the main exception, as our estimate of 28 ± 20 Gg y^{-1} is lower than the 49 Gg y^{-1} reported by Brahney et al. (2021). Overall, this comparison suggests that our methodology preserves the broad regional pattern Brahney et al. (2021), but tends to shift more mass towards several populated or dust-rich continental regions, particularly Russia, Africa, and America.

In contrast, our results deviate much stronger from the substantially higher regional values of Evangeliou et al. (2022). This is apparent for nearly all continental regions. For Asia, our estimate (88 ± 62 Gg y^{-1}) is almost one third of the 250 ± 120 Gg y^{-1} reported by Evangeliou et al. (2022). The same pattern holds for Russia (15 ± 11 vs 44 ± 20 Gg y^{-1}), Europe (28 ± 20 vs 88 ± 42 Gg y^{-1}), North America (41 ± 28 vs 130 ± 55 Gg y^{-1}), South America (16 ± 11 vs 45 ± 22 Gg y^{-1}), and Africa (34 ± 25 vs 110 ± 55 Gg y^{-1}), where our values are significantly smaller, in the range of about 30–35% of the Evangeliou et al. (2022) estimates. Central America shows an even larger relative difference, with our value of 3.4 ± 2.3 Gg y^{-1} compared with 15 Gg y^{-1}, while Oceania is the region where the two studies come closest, since our upper uncertainty range overlaps the 12 ± 5.8 Gg y^{-1} estimate of Evangeliou et al. (2022). The disagreement is especially striking at high latitudes. For Greenland, our estimate is almost negligible (0.004 ± 0.003 Gg y^{-1}), with respect to 18 Gg y^{-1} in Evangeliou et al. (2022), which is a consequence of the correction that we performed for seasonal snow and sea-ice extent and our assumption that atmospheric MPs are not resuspended from snow and sea-ice surfaces (see Section 3.2). Likewise, our Antarctic contribution is zero, in contrast to the non-negligible Antarctic source proposed in Evangeliou et al. (2022). These differences strongly suggest that high-latitude terrestrial sources may have been overestimated in previous inventories. Averaged over the ten land and polar regions, our mean regional emission is about 23 Gg y^{-1}, compared with about 19 Gg y^{-1} in Brahney et al. (2021) and 71 Gg y^{-1} in Evangeliou et al. (2022), about one third smaller.

The comparison with the other studies listed in Table 2 further emphasizes how uncertain the regional MP budget still is. Relative to Fu et al. (2023) for assumed size fractions of 5–70 μm, our estimate (for a slightly larger fraction, 5–100 μm) is slightly higher over Asia, Russia, Europe, North America, Africa, and the ocean, while South America is very similar and Central America and Oceania are somewhat lower. In particular, our estimate for Europe (16 ± 12 Gg y^{-1}) is much larger than the 3.8 Gg y^{-1} reported by Fu et al. (2023), and our oceanic source (443 ± 355 Gg y^{-1}) is twice their 185 Gg y^{-1}. Yang et al. (2025), on the other hand, present an almost opposite regional picture for the same size range (5–70 μm), with extremely large continental emissions across nearly all land regions; for example 3647 Gg y^{-1} in Asia, 2154 Gg y^{-1} in North America, 1511 Gg y^{-1} in Europe, and 943 Gg y^{-1} in Africa, while their oceanic source is only 397 Gg y^{-1}, that is close to ours (443 ± 355 Gg y^{-1}). This leads to a strongly

https://doi.org/10.5194/egusphere-2026-5158
Preprint. Discussion started: 22 September 2026

land-dominated global budget that differs fundamentally from our ocean-dominated distribution. On the contrary, the estimates of Evangelou et al. (2026) are much smaller than ours even when non-spherical particles are included. Under the spherical assumption, total emissions are only 5.155 Gg y^{-1}, and even if films, spheres and cylinders are used for the conversion to mass emissions, they reach only 117.27 Gg y^{-1}, one fifth of our estimate. Thus, Table 2 shows that current regional atmospheric MP emissions span more than three orders of magnitude, reflecting strong sensitivity to the various assumptions made on MP aerosol.

Overall, the regional comparison in Table 2 indicates that our methodology provides an intermediate perspective on the global atmospheric MP source distribution. It is clearly more conservative than the very high previous continental estimates (Evangeliou et al., 2022; Brahney et al., 2021; Yang et al., 2025), but it is not as low as the most restrictive recent inventories. At the same time, it suggests that the earliest estimates may have underestimated emissions in some continental regions, especially Russia, Africa, South America, and parts of North America. Ocean dominates the global source budget, Asia is the principal continental hotspot, North America and Africa are important secondary contributors, and high-latitude land regions such as Greenland and Antarctica contribute negligibly. Our posterior emissions of MPs are, hence, between the extremes currently found in the literature and provide a more balanced view of the global atmospheric MP cycle.

The discussed regional differences in our posterior emissions and those reported elsewhere are further illustrated in Figure 6 providing a spatial explanation for the regional contrasts discussed in Table 2. The figure reveals whether observed mismatches with earlier studies are driven by stronger or weaker hotspot regions or by different land–ocean partitioning of the sources. Compared with Evangeliou et al. (2022) (Figure 6a), the largest differences are clearly associated with the oceanic domain. Broad negative anomalies dominate the ocean, especially across the Southern Ocean and over large parts of the mid-latitude North Pacific and North Atlantic, indicating that our posterior assigns substantially lower emissions to remote marine regions than Evangeliou et al. (2022). Distinct positive mismatches occur over western and central Europe, the Mediterranean basin, and East Asia, implying that our posterior can locally exceed the Evangeliou et al. (2022) estimates even though our regional and global totals are substantially smaller. This suggests that the Evangeliou et al. (2022) inventory is not only larger overall, but also diffuse over the ocean, whereas our posterior is comparatively more concentrated in a limited number of continental and coastal hotspot regions.

The spatial comparison with Fu et al. (2023) (Figure 6b) exhibits a very different structure. Here, MP emissions over most of the globe remain close to ours, and the differences are comparatively weak and spatially localized. The remaining positive mismatches are again concentrated in hotspot areas, particularly Europe/Mediterranean, East Asia, and parts of the North Pacific, while negative differences are generally small and patchy. This indicates that Fu et al. (2023) is one of the inventories that is spatially most similar to our posterior. The disagreement between the two studies appears to be mainly source intensity rather than source location. The geographical structure of the emissions is relatively consistent, but our posterior tends to strengthen several of the major hotspot regions.

https://doi.org/10.5194/egusphere-2026-5158
Preprint. Discussion started: 22 September 2026

On the opposite side, comparison of our posterior with Yang et al. (2025) (Figure 6c) reveals a rather continental mismatch. Strong negative differences cover much of North and South America, Europe, Africa, Southaast Asia, and Australia, which is normal considering that Yang et al. (2025) assigns larger emissions to continental sources (10,000 Gg y^{-1}) than our posterior does. In accordance with Table 2, Yang et al. (2025) exceed our posterior by very large factors in nearly all land regions. Positive mismatches are rare and occur mainly in coastal and marine areas, especially around the Mediterranean and the western North Pacific/East Asian coastal sector. Hence, Figure 6c demonstrates that the disagreement between these emissions reflects a fundamentally different global source partitioning.

The comparison with Evangelou et al. (2026) (Figure 6d) when conversion from number to mass was performed based on the inventory's assumptions on modelled non-spherical shapes and for size fractions spanning 5-100 μm shows small differences. Most of the larger mismatches are positive and centered over Europe/Mediterranean and East Asia. This indicates that the 2026 inventory places several of the main sources in broadly similar regions, but at substantially lower intensity than our posterior. Hence, the main difference in this case appears to be amplitude rather than the overall geographical pattern. The negligible emissions over Greenland and Antarctica are also consistent with our conclusion that ice/snow covered regions do not emit MPs.

5.2 Impact of different size distributions

The main reason for the large discrepancies between our posterior and those reported elsewhere for the mass emissions lies in the size partition of the emitted MPs, and especially in how the coarse fraction of the size distribution is represented, because mass increases much faster with particle size than particle number. Table 3 shows this point clearly. In our posterior, the mass contribution increases from 1.4 ± 1.0 Gg y^{-1} in the 5–10 μm class to 56 ± 43 Gg y^{-1} in 10–25 μm, 187 ± 146 Gg y^{-1} in 25–50 μm, 339 ± 264 Gg y^{-1} in 50–100 μm, and 418 ± 327 Gg y^{-1} in 100–250 μm. Thus, although particles larger than 25 μm account for only one quarter of the emitted particle number in our posterior, they already contribute about 94% of the mass; particles larger than 50 μm represent only about 5% of the particles, yet about 76% of the mass. The contrast is striking for the 100–250 μm fraction, which contributes only 6.5×10^{15} particles y^{-1}, less than 1% of the total particle-number emissions, but accounts for about 42% of the global mass budget. In contrast, the 10–25 μm fraction dominates our particle-number emissions (8.7×10^{17} particles y^{-1}, nearly 60% of the total) but contributes only about 6% of the mass. In other words, the global mass budget is determined primarily by the relatively rare coarse particles, whereas the particle-number budget is controlled by the more abundant fine particles (Figire S6). This asymmetry shows that even modest differences between studies in the abundance, representative diameter, density, or assumed geometry of the coarse fractions are amplified into very large differences in total emitted mass.

That is also why the discrepancies are not removed simply by comparing total emissions across studies without harmonizing size range. In the common 5–100 μm interval, our posterior sums to 583± 454 Gg y^{-1}; the additional 100–250 μm class adds another 418 ± 327 Gg y^{-1}, or about 42% of our global total. However, even when the

https://doi.org/10.5194/egusphere-2026-5158
Preprint. Discussion started: 22 September 2026

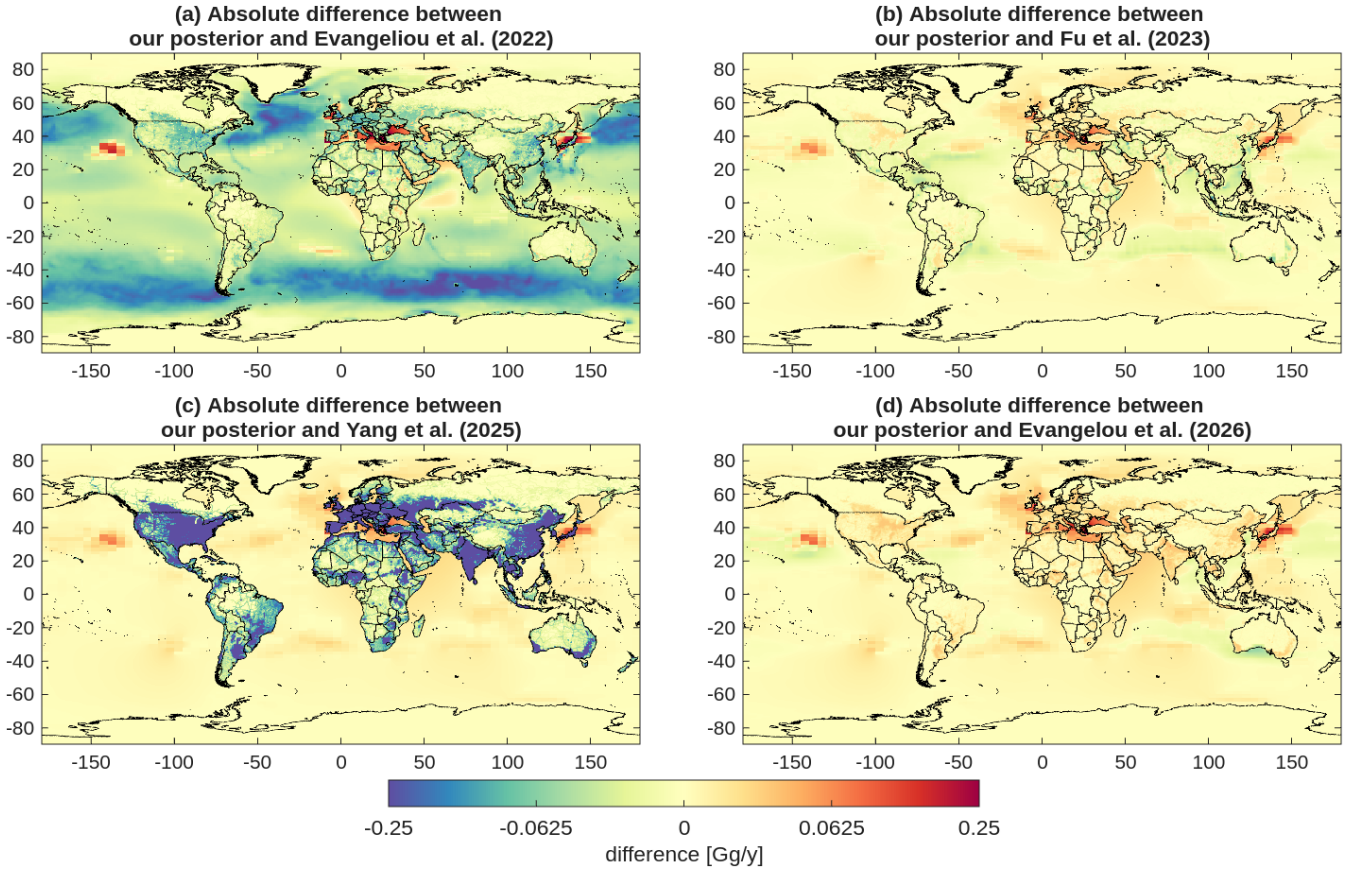

Figure 6. Absolute differences of our current posterior estimates from those reported by (Evangeliou et al., 2022), Fu et al. (2023), Yang et al. (2025) and Evangelou et al. (2026) for the same size fractions reported in Table 2.

comparison is restricted to the common 5–100 μm range, our estimate remains way below the 8700 Gg y^{-1} of Brahney et al. (2021) and the 10328.8 Gg y^{-1} of Yang et al. (2025), and also below the 2618 Gg y^{-1} obtained by summing the 5–100 μm bins of Evangeliou et al. (2022), while it remains above the 322.6 Gg y^{-1} of Fu et al. (2023) and the much smaller recent estimates (Evangelou et al., 2026). Hence, the spread is not caused only by whether studies include larger particles between 100 and 250 μm. It also reflects the different amounts of mass assigned already within the 25–50 and especially the 50–100 μm fractions. Brahney et al. (2021) calculated 7400 Gg y^{-1} in the 50–100 μm class using the same measured size distribution, although they excluded larger particles of 100–250 μm. Using the same distribution, Evangeliou et al. (2022) shifted more mass toward the coarse fraction, with 2000 $\pm$ 920 Gg y^{-1} in 50–100 μm and 7300 $\pm$ 3000 Gg y^{-1} in 100–250 μm assuming spherical geometry, so that almost

https://doi.org/10.5194/egusphere-2026-5158
Preprint. Discussion started: 22 September 2026

all of their global mass budget was driven by particles larger than 50 μm. It is noteworthy that our 100–250 μm contribution alone (418 $\pm$ 327 Gg y^{-1}) exceeds the entire global mass budget reported by Fu et al. (2023)) showing how strongly the upper tail of the size spectrum controls total mass.

In the more recent estimates, Yang et al. (2025), Evangelou et al. (2026) and our posterior showed very similar number emissions in the 50–100 μm fraction spanning $2.1 - 7.4 \times 10^{16}$ particles y^{-1}. However, when using their reported assumptions to convert from number to mass values, Yang et al. (2025) calculates 5868 Gg y^{-1} and Evangelou et al. (2026) 4.56–104 Gg y^{-1} depending on the assumed geometry, in contrast to 339 $\pm$ 264 Gg y^{-1} reported here. The same was seen in the 5–10 μm fraction between Evangelou et al. (2026) and our posterior number emissions of 5.4×10^{17} and 2.2×10^{17} particles y^{-1}, respectively, which is converted to 0.12 Gg y^{-1} if spheres are assumed with respect to our 1.4 $\pm$ 1.0 Gg y^{-1} that is one order of magnitude larger. The largest differences in size distribution are shown for the respective size fractions 10–25 and 25–50 μm, where results are one order of magnitude larger ($3.0 - 8.7 \times 10^{17}$ particles y^{-1}) than those of Evangelou et al. (2026) ($1.1 - 6.6 \times 10^{16}$ particles y^{-1}) and smaller than those of Yang et al. (2025) ($3.3 - 49 \times 10^{17}$ particles y^{-1}).

Note that in Evangelou et al. (2026), when spherical geometry was assumed, the total global mass is only 5.15 Gg y^{-1}, with 4.56 Gg y^{-1} in the 50–100 μm fraction, while when spheres, cylinders, films were considered, the total rises to 117.27 Gg y^{-1}, with 103.78 Gg y^{-1} to be 50–100 μm, even though the particle numbers are the same. This 23-fold increase obtained solely from a change in shape assumption demonstrates that mass budgets are controlled not only by emissions themselves, but also by the conversion from number to particle volume. Accordingly, the large differences between our posterior and the literature should not be interpreted simply as mismatches on source intensity. To a large extent they reflect different assumptions about which size fractions dominate the emissions, how far the coarse fraction extends, and how non-spherical particles are represented when converting number to mass. Our posterior MP emissions are an intermediate estimate within the reported literature spread and its strength is that it is based on measured size fractions for the observations that were used in the inversion algorithm, rather than educational guesses or literature data, such as in more of the recent estimates.

5.3 Comparison with previously-reported continental emissions

Due to the lack of robust analytical techniques for MP analysis, thus comprehensive observations, continental sources have been constrained up to now by bottom up methods. The bottom-up approaches differ from the top-down ones in different type of data inputs and assumptions, which are more focused on local, ground properties. For example, Evangelou et al. (2024) used process understanding of mineral dust emissions obtained in the past decades (Huneeus et al., 2011) to estimate resuspension of MPs from bare soils as a function of MP mass in soil, the enrichment ratio of MPs mass in resuspension relative to MPs mass fraction in the soil, and the previously reported flux of mineral dust by Huneeus et al. (2011). Using this bottom-up approach, Evangelou et al. (2024) estimated the total MPs emissions resuspended from the bare soil to 104 Gg y^{-1} with uncertainty interval 48.3–108.6 Gg y^{-1} for particles between 0.1 and 50 μm. For the same size fraction, our posterior estimate is 0.85–7.64 Gg y^{-1} (Table 4) or more than

https://doi.org/10.5194/egusphere-2026-5158
Preprint. Discussion started: 22 September 2026

one order of magnitude lower. Even our maximum estimate for all studied fractions (5–250 μm), that is 3.4–31.2 Gg y^{-1} (Table 4) is significantly lower that the lowest bound in Evangelou et al. (2024) (31.2 versus 48.3 Gg y^{-1}). Here, our soil resuspension of MPs estimates for regions defined in Figure 4a are compared with those of Evangelou et al. (2024). The same comparison is also depicted for particular regions for quarterly temporal distibutions of MPs emissions in Figure 7. Our estimates for 5–50 μm are significantly lower than those from Evangelou et al. (2024), and only comparable when posterior estimates for all size fractions (5–250 μm) are considered.

As regards to another continental emission sector, namely road dust, Klimont et al. (2017) compiled ground-based in formation of number of automobiles, kilometers driven per year and respective emission factors in the GAINS model and estimated 347 Gg y^{-1} in the PM10 fraction (Table 4). Similar to this, Evangeliou et al. (2020) combined country statistics of tyre weight prior and after use over Scandinavia and Germany and extrapolated globally using CO2 emissions from transportation; they estimated road dust emissions of 237 Gg y^{-1} in the PM10 fraction (Table 4). Our posterior estimate for 5–10 μm particles is two orders of magnitude lower (1.0–4.4 Gg y^{-1}, see Table 4) and this different is best depicted in Figure 7 (note the logarithmic scale). However, when considering total terrestrial emissions, our estimate 238 ± 169 Gg y^{-1} MPs (sum of agriculture, road dust, and soil resuspension) is in a good agreement to those of Fu et al. (2023) who reported total terrestrial sources as 154 Gg y^{-1} with uncertainty bounds 34–688 Gg y^{-1}. This places our mean value slightly higher than their reported estimate, although their upper bound overlaps with our uncertainty range very well. The difference is primarily driven by agricultural emissions, which contribute strongly in our framework but remain minor in their calculation.

5.4 Comparison with previously-reported oceanic emissions

The global MP emissions emitted from the surface of the ocean in the present study were calculated to be 1.1×10^{18} particles y^{-1} for size fractions 5-250 μm, corresponding to mass flux of 763 ± 611 Gg y^{-1}. About 1.6×10^{17} particles y^{-1} were emitted in the 5–10 μm size fraction, corresponding to 0.99 ± 0.79 Gg y^{-1}. For the 10–25 μm size fraction, 6.5×10^{17} particles y^{-1} were emitted, corresponding to 42 ± 33 Gg y^{-1}. In the 25–50 μm range, emissions amounted to 2.2×10^{17} particles y^{-1}, corresponding to 142 ± 113 Gg y^{-1}. For the 50–100 μm size fraction, 5.1×10^{16} particles y^{-1} were emitted, corresponding to 258 ± 206 Gg y^{-1}. Finally, in the 100–250 μm size fraction, 5×10^{15} particles y^{-1} were emitted, corresponding to 319 ± 255 Gg y^{-1}. Overall, while the number of emitted particles decreases with increasing particle size, the associated mass emissions increase substantially, reflecting the strong dependence of particle mass on diameter and shape.

Our calculated oceanic MP emissions were complemented against emissions from the relevant literature in Table 5. In the very first study, Allen et al. (2020) analysed air samples with micro-Raman spectroscopy in the marine boundary layer on the French Atlantic coast during both onshore (average of 2.9 particles m^{-3}) and offshore (average of 9.6 particles m^{-3}) winds. They further showed a potential for MPs to be released from the marine environment into the atmosphere extrapolating into a global annual flux of 136 Gg y^{-1} of 5–140 μm blowing on shore.

https://doi.org/10.5194/egusphere-2026-5158
Preprint. Discussion started: 22 September 2026

Table 4. Emissions from continental sources in different continents. Top part of the table shows emissions of atmospheric MPs for bare soil resuspension from Evangelou et al. (2024) and from this study. Bottom part shows emissions of atmospheric road dust estimated by Evangeliou et al. (2020), Klimont et al. (2017), and this study.
⋆ Soil resuspension; ⋆⋆ Road dust

MPs [Gg/y]	Asia	Russia	Greenland	Europe	N. and C. Amer.	S. Amer.	Africa	Oceania	Total
Evangelou et al. (2024)⋆	27.1-61.5	0.032-0.11	0.0003-0.001	0.18-0.41	1.25-3.2	0.45-1.8	18.6-42	0.011-0.036	48.3-108.6
this study (5-50 μm)⋆	0.35-3.16	0.007-0.06	0.0002-0.0019	0.002-0.019	0.018-0.16	0.019-0.17	0.43-3.85	0.0076-0.068	0.85-7.64
this study (5-250 μm)⋆	1.42-12.93	0.027-0.25	0.0009-0.008	0.009-0.08	0.072-0.66	0.077-0.70	1.73-15.72	0.031-0.28	3.4-31.2
Evangeliou et al. (2020)⋆⋆	87.6	2.52	0	35.7	64.9	16.6	12.9	3.43	237
Klimont et al. (2017)⋆⋆	112.5	9.21	0	50.2	107.9	23.5	15.7	5.31	347
this study⋆⋆	0.43-1.84	0.008-0.034	0	0.13-0.57	0.29-1.23	0.09-0.38	0.07-0.28	0.02-0.07	1.038-4.404

Except for Brahney et al. (2021) and Evangeliou et al. (2022) who reported oceanic emissions of MPs almost an order of magnitude larger than our posterior ones here, Yang et al. (2022) conducted laboratory experiments of the transfer of MPs from the water surface to the atmosphere and found that MPs were highly enriched in the atmosphere relative to seawater, with experimentally determined enrichment factors reaching 24,000 depending on the size of MPs. These results were used for a bottom-up calculation of oceanic emissions of MP for particle diameters of 0.3–70 μm. They reported an annual global flux of 24×10^{18} particles y^{-1} (1–47×10^{18} particles y^{-1}), corresponding to 0.773 Gg y^{-1} (0.03–1.515 Gg y^{-1}). For MP with diameters of <10 μm that are subject to long-range atmospheric transport, they reported that 23×10^{18} particles y^{-1} (1–45×10^{18} particles y^{-1}) or 0.039 Gg y^{-1} (0.002–0.076 Gg y^{-1}) were emitted. We report that 1.6×10^{17} particles y^{-1} or 0.99 ± 0.79 Gg y^{-1} for the 5–10 μm particles.

Later, Harb et al. (2023) conducted laboratory experiments to understand the impact of size, density, and concentration of MPs in water on their aerosolization. Their results showed that the <10 μm diameter MPs considered can be emitted via bubble bursting, with the aerosolization increasing monotonically with an increase in the concen-

https://doi.org/10.5194/egusphere-2026-5158
Preprint. Discussion started: 22 September 2026

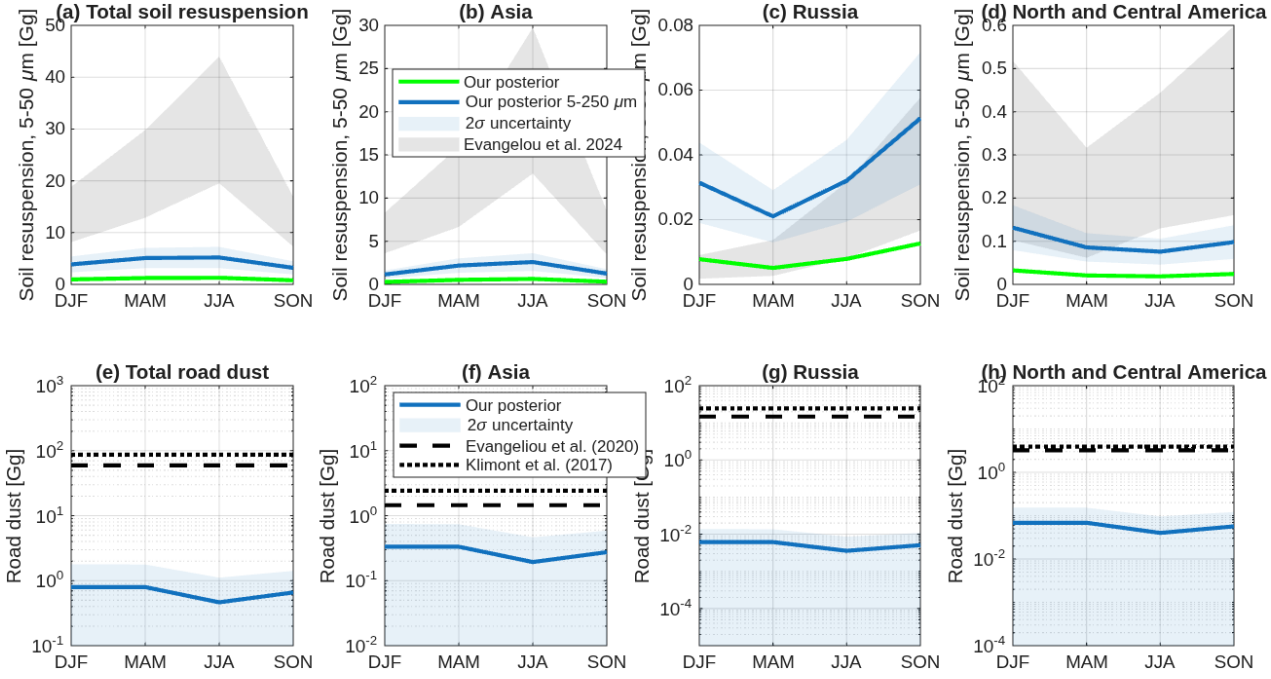

Figure 7. Top: comparison of atmospheric MPs emissions resuspended from bare soils estimated in this study and those of Evangelou et al. (2024) for bare soil resuspension for Asia, Russia, and North and Central America. Our estimates are given using full green lines for our posterior 5-50 μm (consistent with Evangelou et al. (2024)), full blue lines for our posterior 5-250 μm associated with 2 standard deviation, i.e. 95% confidence intervals, using blue areas while those of Evangelou et al. (2024) are given as their reported uncertainty bounds using gray regions. Bottom: comparison of MPs emissions from road dust for the 5-25 μm fraction against the estimates of Evangeliou et al. (2020) and Klimont et al. (2017).

tration in water and decreasing with an increase in the particle size. They estimated oceanic emissions for <10 μm particles (0.5, 2, and 10 μm) to be 0.00166 Gg y^{-1}, with uncertainty bounds between 0.00072 and 0.00413 Gg y^{-1}. This corresponds to 51×10^{15} particles y^{-1}, which is almost two orders of magnitude lower than the flux reported here for the 5–10 μm fraction (1.6×10^{17} particles y^{-1}).

Fu et al. (2023) used global atmospheric abundance data, GEOS-Chem atmospheric model adapted to model MPs, and optimal estimation to constrain the atmospheric sources. They reported that the global atmospheric MP emissions are 324 (73–1,450) Gg y^{-1}. The ocean sources were estimated to have a rather small contribution to global emission of 171 (38–764) Gg y^{-1} , followed by road-related sources (115 [26–513] Gg y^{-1}) including the suspension of tire and brake wear and mismanaged plastic waste. They simulated 0.3–70 μm size particles stating that 99% of them were coarse ones, further reporting a net land-to-ocean transport by the atmosphere equal to 25 Gg y^{-1}. Our posterior annual fluxes for size fractions <50 μm are equal to 43 ± 34 Gg y^{-1}, almost one fifth their emissions.

https://doi.org/10.5194/egusphere-2026-5158
Preprint. Discussion started: 22 September 2026

Atmospheric MPs emissions from the ocean were also calculated by Shaw et al. (2023) demonstrating a mechanistic study of bursting bubbles transporting MPs. Their study focused on particle size ranges from 0.5 to 280 μm. They reported that jet drops are efficient at emitting MPs up to 280 μm in diameter dominating the emitted mass. The results were extrapolated to provide a global calculation with respect to bubble scavenging and bursting physics, local wind and sea state, and oceanic MP concentrations. They found annual emissions ranging from 20 to 7,400 Gg y^{-1} (best guess 100 Gg y^{-1}). Our corresponding estimate for 10–250 μm particles is 762 $\pm$ 610 Gg y^{-1}.

Bucci et al. (2024) presented a bottom-up assessment of sea-spray-driven atmospheric emissions based on a combination of a sea-salt emission parameterization from Grythe et al. (2014) and an ocean transport model Richon et al. (2022). Their analysis considers particle diameters between 1 and 60 μm. To ensure consistency, we restrict the comparison to the overlapping 5–50 μm size range. For this size fraction, substantial differences are found between the two emissions. In the Northern Hemisphere, our estimate amounts to 146 $\pm$ 117 Gg y^{-1}, whereas Bucci et al. (2024) reported only 0.0318 Gg y^{-1} (uncertainty range: 0.0083–0.139 Gg y^{-1}). Similarly, for the Southern Hemisphere, our estimate of 38 $\pm$ 31 Gg y^{-1} exceeds their value of 0.0149 Gg y^{-1} (range: 0.0039–0.065 Gg y^{-1}). Thus, our top-down estimates are approximately three to four orders of magnitude larger than the bottom-up results of Bucci et al. (2024). These discrepancies likely reflect fundamental differences between the methodologies. While Bucci et al. (2024) derive emissions from simulated ocean concentrations combined with sea-spray parameterizations, our inversion is constrained by atmospheric observations (though not directly taken above the ocean), suggesting substantially larger ocean–atmosphere fluxes.

Yang et al. (2025) used the Model for Ozone and Related Species version 4 (MOZART-4) for 2013–2014 and assumed different atmospheric MPs emissions magnitudes compared to most of previous studies. The total MPs they estimated is dominated by tires, brakes, and agricultural sources (10,000 Gg y^{-1}), accompanied by smaller contributions from dust and soil (300 Gg y^{-1}) and an almost negligible flux of oceanic MPs (0.8 Gg y^{-1}). The particularly low oceanic contribution reflects their explicit adoption of recent mechanistic sea–air transfer studies (Yang et al., 2022; Harb et al., 2023; Shaw et al., 2023), which emphasize the inefficiency of bubble bursting as a pathway for MPs release to the atmosphere. Using a number-based size distribution of atmospheric microplastics, they extrapolated the calculated MP concentrations of 0.5–70 μm size range to the concentrations of particles observed in all the size ranges and validated their model simulation results using these emissions. Our posterior emissions for 5–50 μm size were estimated to be are equal to 43 $\pm$ 34 Gg y^{-1}.

Finally, Evangelou et al. (2026) compiled 925 atmospheric concentration, 1,007 bulk deposition, 556 wet deposition and 294 dry deposition measurements collected during the period from 2014 to 2024. They further applied a simple scaling method estimating that the total global land-based and oceanic emissions were 6.1×10^{17} ($1.3–11\times10^{17}$) particles y^{-1} and 2.6×10^{16} ($0.27–5.0\times10^{16}$) particles y^{-1}, respectively. While they have used non-spherical shapes (e.g., cylinders) to simulate transport of MPs in this measurement dataset, they converted number to mass concentrations assuming spheres (Evangelou et al., 2026) amounting 4 (0.5–8) Gg y^{-1} for 5–100 μm particles, which implies an underestimation as if cylinders had been assumed. In addition, the compilation of this large dataset of MP mea-

https://doi.org/10.5194/egusphere-2026-5158
Preprint. Discussion started: 22 September 2026

surements, while helpful, is not consistent; it is composed of samples measured with Stimulated Raman Scattering (SRS), Scanning Electron Microscopic (SEM), Energy Dispersive X-ray (EDX), Fourier-Transform Infrared (FTIR), Attenuated Total Reflectance (ATR), Pyrolysis-Gas Chromatography/Mass Spectrometry (py-GC/MS), Laser Direct Infrared (LDIR) and μ-Raman spectroscopic techniques. Primpke et al. (2020) compared various methods and instruments based either on spectroscopy or thermoanalytical methods applied to the same environmental samples. They reported that even after a data harmonization step, while the overall trends in MP contamination were very similar, differences were observed in the polymer compositions. Gaston et al. (2020) explored airborne MPs inside and outside of buildings in California by filtering known volumes of air through glass fiber filters, which were then subsequently characterized with a variety of microscopy techniques painting different pictures of airborne plastic compounds. Recently, Aves et al. (2026) compared five analytical methods for MP analysis (Fluerescence, FTIR, Raman, TD-PTR-MS, Py-GC/MS) and found that their results are not directly comparable because they differ in particle detection, polymer identification, reporting units, and sensitivity. They concluded that comparisons should only be made between studies using the same analytical method. Specifically, different methods identified different polymer types with minimal overlap. Raman detected 19 polymer types, while TD-PTR-MS and Py-GC/MS each identified only four. Py-GC/MS detected 10 times higher concentrations than TD-PTR-MS, highlighting huge differences even between chemical methods. Fluorescence microscopy identified concentrations over 13 times higher than Raman and showed systematic disagreement with all chemical methods (TD-PTR-MS and Py-GC/MS), raising concerns about its reliability for MP quantification.

This comparison highlights the uncertainty of water–air exchange processes and demonstrates how different methodological choices, such as relying on laboratory-based parameterizations in bottom-up approach and the use of measurements for constraining using inverse methodologies, can lead to very large discrepancies in estimation of global atmospheric MPs budget. While results of Yang et al. (2025) fall outside the range of most other current estimates, they provide an important boundary case that highlights the need for better constraints on the physical mechanisms of oceanic emissions.

5.5 Can oceanic emissions of MPs be near-zero?

In recent years, experiments on emissions of MPs from water to air, mainly through bubble bursting, sea-spray aerosol generation, plus a smaller set on raindrop splash ejection have been performed. The injection mechanism is such that bubbles scavenge particles while rising, burst at the surface, and eject film drops or jet drops that may contain microplastics. Droplets then evaporate, leaving airborne plastic particles suspended in the atmosphere. Jet drops create larger droplets and thus mass, while film drops are important for smaller aerosol number (Shaw et al., 2023). Masry et al. (2021) conducted direct laboratory experiments and provided evidence that bubble bursting can transfer plastic particles from water to air. Under their laboratory conditions, transfer was possible and mainly for smaller particles. Catarino et al. (2023) examined micro-nano-plastic (MNP) aerosolization under controlled wave conditions and reported up to 18,809 particles mL^{-1} for 0.5 μm beads with 19 times enrichment, and 1,977 particles

https://doi.org/10.5194/egusphere-2026-5158
Preprint. Discussion started: 22 September 2026

Table 5. Summary of literature estimates for ocean-to-atmosphere microplastic emissions.

Study	Ocean → atmosphere pathway / method	Particles / y	Gg / y	Size range
Allen et al. (2020)	Coastal measurements + coastline extrapolation ("blown onshore")	—	135.995	5–140 μm
Brahney et al. (2021)	Top-down inversion (W. US deposition) with global extrapolation	—	$\approx$ 8600 (0–22000)	0.3–70 μm
Evangeliou et al. (2022)	Top-down inversion (W. US deposition) with global extrapolation	—	8900 (5400 12400)	5–250 μm
Yang et al. (2022)	Bottom-up sea-spray formation + global scaling	24 (1–47)$\times 10^{18}$	0.773 (0.003–1.515)	0.3–70 μm
Harb et al. (2023)	Lab sea-spray emission parameterization scaled globally	50.7 (14.2–93.4$\times 10^{15}$)	0.00166 (0.00072–0.00413)	$\leq 10\mu$m
Fu et al. (2023)	GEOS-Chem MP model + optimal estimation	—	171 (38–764)	0.3–70 μm
Shaw et al. (2023)	Bubble jet-drop scavenging + global scaling	—	20–7400	Lab: 10–280 μm
Bucci et al. (2024)	Bottom-up sea-spray emission (sea-salt parameterization + ocean MP transport model)	—	1.231 (0.320 5.383)	1–60 μm
Yang et al. (2025)	Assumed low emissions, then fed to a model and extrapolated to all sizes for validation	—	0.8	1–70 μm
Evangelou et al. (2026)	Scaled bottom-up emissions (aligned to modeled size bins)	2.6$\times 10^{16}$ (0.27–5.0$\times 10^{16}$)	4 (0.5–8)	5–100 μm
This study	Top-down inversion (W. US deposition) with global extrapolation	1.1×10^{18}	763 (152 1375)	5–250 μm

mL^{-1} for 10 μm beads with twofold enrichment. Harb et al. (2023) performed experiments using a seaspray tank and showed that aerosolization increased with water concentration and decreased with particle size. Floating polyethylene (PE) aerosolized less effectively than suspended polystyrene (PS). They estimated maximum oceanic emissions of 50.7×10^{15} particles y^{-1} or 1.66 t y^{-1} for the MNP size range. Oehlschlägel et al. (2024) produced bubbles with filtered air that was pushed through a stainless-steel frit at two different flow-rates in a glass flask filled with PS particles of six diameters. Airborne MP concentrations ranged 4.2–348 particles L^{-1}. They reported that MP particles up to 1 μm were enriched in jet droplets relative to bulk water. Shaw et al. (2023) used two high-speed cameras to record a single

https://doi.org/10.5194/egusphere-2026-5158
Preprint. Discussion started: 22 September 2026

bubble bursting. They showed that jet drops can eject MPs when particles are similar to or smaller than the jet-drop size. Lambert et al. (2024) used a laboratory-based bubble bursting mechanism, simulating the aerosolization process at sea to investigate the influence of MPs as well as seawater characteristics. They found that enrichment depends on size, concentration, polymer type, and seawater properties. Smaller and denser particles tended to enrich more. Kjærgaard et al. (2024) used a laboratory setting for low salinity waters to elucidate the emission of submicron PS by bubble bursting. They showed that bubble bursting can generate airborne MPs, aerosol production scaled linearly with plastic number concentration in water, while small salt additions increased production. Polymer composition was confirmed by filter analysis using Py-GC/MS. Pokhrel and Foroutan (2026) conducted controlled experiments with 1 μm diameter surface-modified PS MPs of two contrasting wettabilities (i.e., hydrophilic vs. hydrophobic) in ultrapure water. Film and jet drop pathways were isolated by generating two distinct bubble populations known to primarily produce each droplet type. They reported that hydrophobic MPs had about one order of magnitude higher aerosolization factor than hydrophilic MPs, while film drop aerosolization showed no significant wettability difference. This suggests surface properties can strongly affect which plastic polymers are emitted. Finally, Lehmann et al. (2021) combined simulations and experimental measurements to investigate whether droplets can remobilise MP particles with diameters of a few tens of μm from ocean water to the atmosphere. They reported that a 4 mm raindrop impact ejected more than 167 droplets on average, while laboratory experiments confirmed MP in spray. They estimated around 4,800 MP particles particles km^{-2} h^{-1} entering air during rainfall at 10 mm h^{-1} rain and 0.5 m s^{-1} updraft.

Almost all the aforementioned studies confirm that MPs can be resuspended from the surface of the ocean. Particle size is the dominant driver of MP resuspension. Smaller particles are aerosolized more efficiently in many tank studies, whereas larger particles may still be ejected by larger jet drops, especially in single-bubble physics experiments. Particle properties such as density, wettability, aggregation, aging, and polymer composition affect aerosolization. For instance, floating PE can behave differently from suspended PS, hydrophobicity can enhance jet-drop transfer and seawater composition can change transfer rates. To show that our top-down oceanic emissions cannot be near-zero, such as in recent studies (Evangelou et al., 2026), we have isolated samples taken in oceanic regions, usually with ship campaigns, from the independent observation dataset. We further calculated modelled concentrations using all available gridded emission inventories for MPs (our posterior, (Fu et al., 2023; Yang et al., 2025; Evangelou et al., 2026)). Figure 8a shows the spatial distribution of the observations taken in the ocean and the corresponding SRMs of the samples. The latter further shows that the air arriving at the selected oceanic stations at the time of sampling is largely of oceanic origin, except for some coastal stations in North Europe and China. The comparison of modelled concentrations with these observations is depicted in Figure 8b. Our posterior emissions produce modelled MP concentrations for which 60% within an order of magnitude from the observations, while 19% are outliers differing by more than two orders of magnitude. The emissions from Evangelou et al. (2026) result in 50% of the modelled oceanic concentration falling within an order of magnitude from the observations with 26% classified as outliers For cylindrical shapes, Yang et al. (2025) resulted in 33% of modelled MPs within a 10-fold

https://doi.org/10.5194/egusphere-2026-5158
Preprint. Discussion started: 22 September 2026

difference from the observations with 29% to be outliers. Simulations assuming spherical shapes performed even worse, with only 31% of concentrations within one order of magnitude from the observations and 49% differing by more than two orders of magnitude. Finally, Fu et al. (2023) showed a similar level of agreement with 31% of modelled concentrations within a 10-fold difference from the observations and 25% classified as outliers. Box & Whisker plots of monthly observations and modelled concentrations using the aforementioned five emission datasets are illustrated in Figure 8c. At a first glance, the emissions of Yang et al. (2025) assuming spherical particles (purple) produce concentrations that are 10–20 times higher than the measurements (black) in all months. The emissions from Fu et al. (2023) and Yang et al. (2025) for cylinders (red and yellow, respectively) show somewhat better agreement with the observations during some months (e.g., March, November, December). Emissions from Evangelou et al. (2026) (green) result in concentrations that are much closer to the observations. However, they exhibit variability spanning nearly two orders of magnitude in some months (March, November). In contrast, our posterior emissions show both good agreement with the observations and small monthly variability.

Following the recent findings by Yang et al. (2025) and Evangelou et al. (2026), who argued that the ocean contributes only a negligible share to global MPs emissions, we performed an additional sensitivity experiment. We scaled our posterior oceanic emissions downwards by a factor of 10 and scaled the road transport emissions upwards by the same factor to match that (a) oceanic emissions are almost negligible, and (b) road dust emissions are the largest atmospheric MP contributors, as indicated by observations (Latz et al., 2026; Herzke et al., 2025; Jurkschat et al., 2025; Goßmann et al., 2023). This resulted in only 76.3 Gg y^{-1} of oceanic emissions, 511 Gg y^{-1} of road dust, 170 Gg y^{-1} of bare soils and 17 Gg y^{-1} of agricultural ones and a total annual sum of 774 Gg. Then we coupled the ”scaled” posterior emissions with the SRMs corresponding to the oceanic observations and plot the comparison in Figure S7. The scaled posterior emissions result in modelled concentrations that are Our posterior emissions produce modelled MP concentrations that are only 38% within an order of magnitude from the observations, while 30% of the scaled posterior concentrations differ from the observations by more than two orders of magnitude. Note that the modelled concentrations resulting from our posterior emissions of atmospheric MPs that are presented in this study were 60% within an order of magnitude from the observations with 19% to be more than two orders of magnitude different. In addition, modelled MP concentrations from the scaled posterior emissions were the lowest in all months except March (Figure S7h). Despite these clear findings showing that negligible oceanic emissions cannot force modelled concentrations close to atmospheric observations above the ocean or at coastal sites, more measurements are needed during ship cruises or even airplane campaigns. However, the fact that a robust analytical methodology, that would require low sample volumes or even online measurements of microplastics currently limits further expansion of atmospheric MP observations.

https://doi.org/10.5194/egusphere-2026-5158
Preprint. Discussion started: 22 September 2026

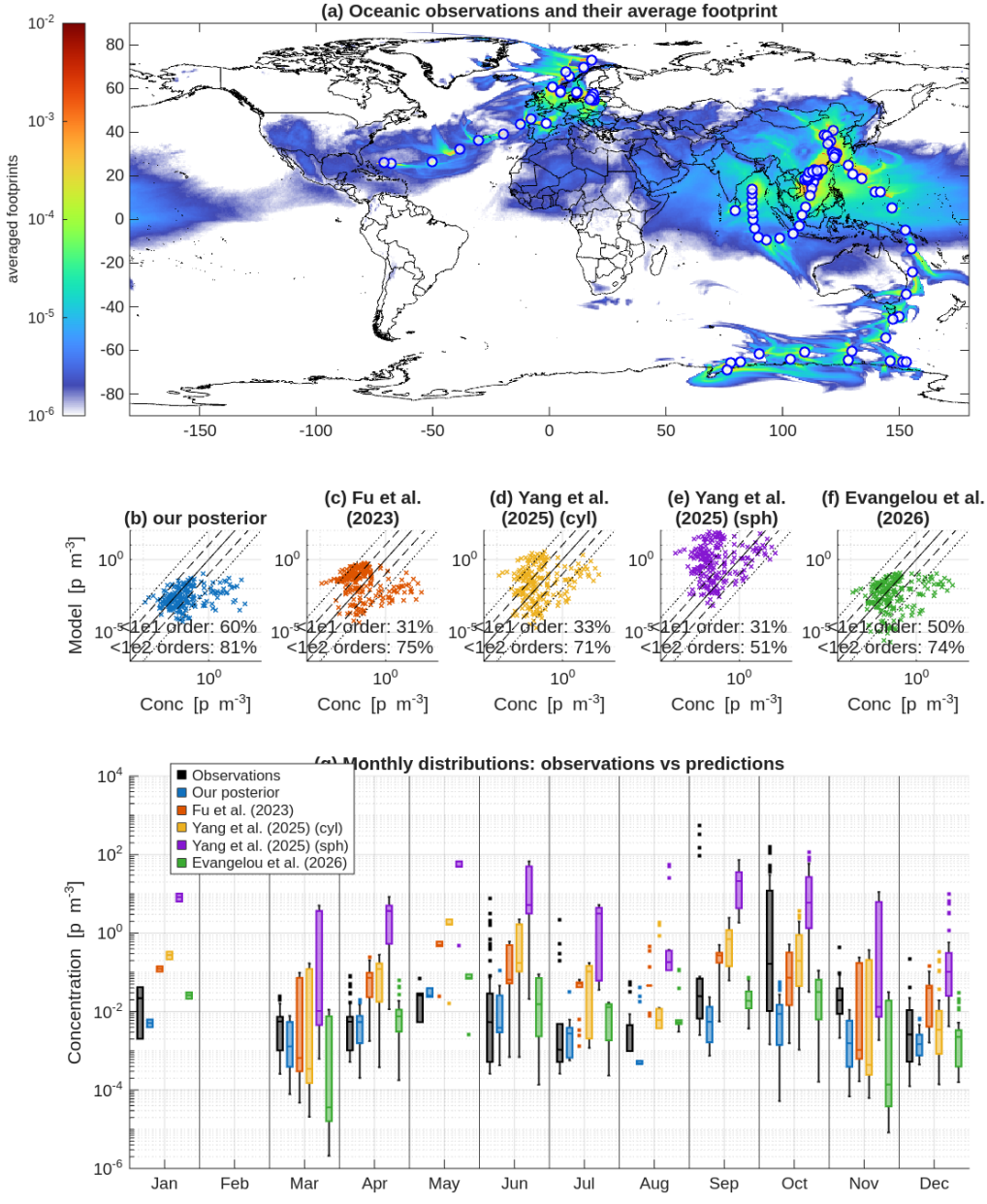

Figure 8. (a) Global distribution of ocean concentration measurements used in this study (white circles) together with their corresponding averaged model footprints. (b–f) Comparison between observed and reconstructed MPs concentrations over the ocean for (b) our posterior estimate, (c) (Fu et al., 2023), (d) (Yang et al., 2025) assuming cylindrical particles, (e) (Yang et al., 2025) assuming spherical particles, and (f) (Evangelou et al., 2026), accompanied by the fraction of predictions within one and two orders of magnitude of the observations. (g) Associated monthly distributions of observed and modeled concentrations.

https://doi.org/10.5194/egusphere-2026-5158
Preprint. Discussion started: 22 September 2026

6 Conclusions

In this study, we used pattern-restricted Bayesian inversion to constrain emissions of atmospheric MPs from wet and dry deposition observations at remote sites of the western United States. To reduce the ill-conditioned global inverse problem, emissions were restricted to four source patterns representing agricultural activity (plastic nets), bare soil resuspension, road dust, and oceanic resuspension. This is a fair assumption, as hotspots of MP emissions, particularly for larger particles, are expected to occur close to their sources, namely marine garbage patches (oceanic emissions), dry desert regions (bare soil resuspension), roads with high traffic volumes (road dust) and, intense agricultural areas (agricultural emissions). The respective uncertainties of the posterior MP emissions were estimated using the Gibbs sampler combined with an orthogonal transformation of the inverse problem, allowing a probabilistic characterization of source strengths while enforcing non-negative emissions.

For the western US inversion domain, the inferred annual MP emissions were 12.15 ± 8.45 million particles m^{-2} y^{-1}, corresponding to 18.69 ± 13.10 Gg y^{-1} under a measured particle density, size distribution, and shape representation. The posterior reconstruction reproduced the observed deposition variability reasonably well, with a Pearson correlation coefficient of 0.537 between measured and reconstructed deposition rates. When the posterior emissions were extrapolated on a global scale, we estimated total global atmospheric MP emissions of 1.46×10^{18} particles y^{-1}, equivalent to 1001 ± 781 Gg y^{-1} for particles between 5 and 250 μm. This emission rate is lower than several previous top-down inventories, but higher than some recent bottom-up estimates. The global budget was dominated by oceanic emissions, which contributed 1.11×10^{18} particles y^{-1}, or 763 ± 611 Gg y^{-1}, corresponding to approximately 75% of the total emitted mass. Terrestrial emissions were also substantial, with agriculture contributing 170 ± 125 Gg y^{-1}, road dust 51 ± 31 Gg y^{-1}, and bare soil resuspension 17 ± 14 Gg y^{-1}.

At a regional scale, the ocean was the largest global source region, while Asia was the dominant continental source, followed by North America, Africa, Europe, South America, Russia, Oceania, and Central America. Greenland contributed negligibly and Antarctica contributed zero emissions in the present framework, consistent with the assumption that MPs are not resuspended from snow- and ice-covered surfaces. These results suggest that densely populated, intensively cultivated, and highly urbanized regions are key continental hotspots, whereas arid regions contribute through dust/soil resuspension.

The inferred size distribution showed a strong decoupling between particle number and emitted mass. The 10–25 μm size class dominated particle number emissions, whereas the mass budget was controlled mainly by larger particles. Particles >50 μm represented only a small fraction of the emitted particle number but accounted for most of the emitted mass. This demonstrates that assumptions about particle size, density, and geometry are critical when converting between particle number and mass emissions. Differences in these assumptions explain a substantial part of the spread among published atmospheric MP emission datasets.

Independent validation against global atmospheric MP concentration and deposition measurements showed that our posterior emissions captured the observed variability. The comparison resulted in a Spearman correlation co-

https://doi.org/10.5194/egusphere-2026-5158
Preprint. Discussion started: 22 September 2026

efficient of 0.57 and a geometric mean bias of 0.21, indicating an overall underestimation but a good correlation between modelled and observed values. Half of the modelled values were within one order of magnitude of the observations, and 88% within two orders of magnitude. A separate comparison against measurements taking during ship campaigns in the World Ocean further confirmed that oceanic emission cannot be near-zero. Our posterior inventory reproduced a large fraction of oceanic observations much better than several alternative inventories.

Posterior uncertainty was dominated by the statistical spread of the Bayesian inversion rather than by the sensitivity to the tested wet-scavenging parameterizations. Although wet removal remains poorly constrained for MPs, since scavenging coefficients for MPs have not been measured yet, and represents an important physical uncertainty, the range of low, medium, and high scavenging scenarios produced smaller variability than the posterior uncertainty from the Gibbs sampler. This suggests that, within the assumptions of the present study, the largest uncertainties arise from the limited observational constraints, the fixed source-pattern assumption, and the inverse estimation.

Several limitations should be considered when interpreting these results. First, the inversion is constrained primarily by measurements from the Western United States, and the global extrapolation depends strongly on the assumed source patterns. Second, the spatial distributions within each of the four emission sectors are prescribed rather than inferred independently. Third, the conversion from particle number to mass depends on assumptions about particle size, density, and shape that were made when modelling MPs. Fourth, wet scavenging of MPs remains experimentally unconstrained even though it does not seem to contribute to the estimated posterior uncertainty. Finally, independent validation datasets, that are used to infer emissions (e.g., Evangelou et al., 2026) or compared with model results, include measurements obtained using different analytical methodologies. Such measurements have shown to differ substantially, not only on the total MP number/mass, but also in the polymer distribution across the same sample introducing additional uncertainty.

Despite these limitations, this study provides a probabilistic, observation-constrained (top-down) estimate of global atmospheric MP emissions. The results indicate that oceanic emissions are likely important, but not to the extent suggested in earlier studies, and that terrestrial sources, especially agriculture and road dust, make a substantial contribution to the atmospheric MP burden. Future progress requires harmonized long-term measurements across continents and oceans, improved size and shape observations, direct experiments of scavenging coefficients, and better understanding of ocean–atmosphere and land–atmosphere MP exchange. These developments are crucial for reducing uncertainties in the global atmospheric MP cycle if we aim at assessing environmental and climatic implications of emerging contaminants.

Code availability. Post-processing code is available upon request to O. Tichý (otichy@utia.cas.cz)

https://doi.org/10.5194/egusphere-2026-5158
Preprint. Discussion started: 22 September 2026

Data availability. Posterior emissions of atmospheric MPs are publicly available from https://doi.org/10.82160/c8h5-rm98. FLEXPART model output is available upon request to N. Evangeliou (ne@nilu.no).

Supplement. The supplement related to this article is available online at +++

Author contributions. OT performed the analysis and wrote the paper. VK and VS assisted the inverse modelling development and analyses. NE designed, coordinated and wrote the paper. SE assisted in data analysis. All authors contributed to the final version.

Competing interests. The authors declare that the do not have any competing interests.

Disclaimer. Publisher's note: Copernicus Publications remains neutral with regard to jurisdictional claims made in the text, published maps, institutional affiliations, or any other geographical representation in this paper. While Copernicus Publications makes every effort to include appropriate place names, the final responsibility lies with the authors. Views expressed in the text are those of the authors and do not necessarily reflect the views of the publisher.

Financial support. This research has been supported by the Czech Science Foundation, grant no. GA24-10400S. NE and SE were financially supported by the Norwegian Research Council (NFR) project MAGIC (Airborne Microplastic Detection, Origin, Transport and Global Radiative Impact, Project No. 334086). FLEXPART simulations are cross-atmospheric research infrastructure services provided by ATMO-ACCESS (EU grant agreement No 101008004).

Acknowledgements. We acknowledge Dr. I. Evangelou (University of Vienna, Austria) for providing the observations used in the independent validation. The computations/simulations were performed on resources provided by Sigma2 - the National Infrastructure for High Performance Computing and Data Storage in Norway (NN10030K/NS10030K).

https://doi.org/10.5194/egusphere-2026-5158
Preprint. Discussion started: 22 September 2026

References

Allen, S., Allen, D., Moss, K., Le Roux, G., Phoenix, V., and Sonke, J.: Examination of the ocean as a source for atmospheric microplastics, PloS one, 15, e0232 746, https://doi.org/10.1371/journal.pone.0232746, 2020.

Aves, A., MacDonald, A., Naeher, S., Materic, D., Castle, D., Davy, P., Gaw, S., and Revell, L.: Comparative assessment of five analytical methods for airborne microplastics highlights importance of identifying sub-10 μm methods, Scientific Reports, https://doi.org/10.1038/s41598-026-49405-2, 2026.

Bakels, L., Tatsii, D., Tipka, A., Thompson, R., Dütsch, M., Blaschek, M., Seibert, P., Baier, K., Bucci, S., Cassiani, M., et al.: FLEXPART version 11: Improved accuracy, efficiency, and flexibility, Geoscientific Model Development, 17, 7595–7627, https://doi.org/10.5194/gmd-17-7595-2024, 2024.

Bergmann, M., Mützel, S., Primpke, S., Tekman, M. B., Trachsel, J., and Gerdts, G.: White and wonderful? Microplastics prevail in snow from the Alps to the Arctic, Science advances, 5, eaax1157, https://doi.org/10.1126/sciadv.aax1157, 2019.

Bocquet, M.: Parameter-field estimation for atmospheric dispersion: application to the Chernobyl accident using 4D-Var, Quarterly Journal of the Royal Meteorological Society, 138, 664–681, https://doi.org/10.1002/qj.961, 2012.

Brahney, J., Hallerud, M., Heim, E., Hahnenberger, M., and Sukumaran, S.: Plastic rain in protected areas of the United States, Science, 368, 1257–1260, https://doi.org/10.1126/science.aaz581, 2020.

Brahney, J., Mahowald, N., Prank, M., Cornwell, G., Klimont, Z., Matsui, H., and Prather, K.: Constraining the atmospheric limb of the plastic cycle, Proceedings of the National Academy of Sciences, 118, https://doi.org/10.1073/pnas.2020719118, 2021.

Brožová, A., Šmídl, V., Tichý, O., and Evangeliou, N.: Spatial-temporal Source Term Estimation using Deep Neural Network Prior and its Application to Chernobyl Wildfires, Journal of Hazardous Materials, p. 137510, https://doi.org/10.1016/j.jhazmat.2025.137510, 2025.

Bucci, S., Richon, C., and Bakels, L.: Exploring the transport path of oceanic microplastics in the atmosphere, Environmental Science & Technology, 58, 14 338–14 347, https://doi.org/10.1021/acs.est.4c03216, 2024.

Casella, G. and George, E. I.: Explaining the Gibbs Sampler, The American Statistician, 46, 167–174, https://doi.org/10.1080/00031305.1992.10475878, 1992.

Catarino, A. I., León, M. C., Li, Y., Lambert, S., Vercauteren, M., Asselman, J., Janssen, C. R., Everaert, G., and De Rijcke, M.: Micro-and nanoplastics transfer from seawater to the atmosphere through aerosolization under controlled laboratory conditions, Marine Pollution Bulletin, 192, 115 015, https://doi.org/10.1016/j.envpol.2021.116949, 2023.

Chib, S. and Greenberg, E.: Understanding the Metropolis-Hastings Algorithm, The American Statistician, 49, 327–335, https://doi.org/10.1080/00031305.1995.10476177, 1995.

De Meutter, P. and Delcloo, A.: Uncertainty quantification of atmospheric transport and dispersion modelling using ensembles for CTBT verification applications, Journal of environmental radioactivity, 250, 106 918, https://doi.org/10.1016/j.jenvrad.2022.106918, 2022.

Eckhardt, S., Cassiani, M., Evangeliou, N., Sollum, E., Pisso, I., and Stohl, A.: Source–receptor matrix calculation for deposited mass with the Lagrangian particle dispersion model FLEXPART v10. 2 in backward mode, Geoscientific Model Development, 10, 4605–4618, https://doi.org/10.5194/gmd-10-4605-2017, 2017.

https://doi.org/10.5194/egusphere-2026-5158
Preprint. Discussion started: 22 September 2026

Eckhardt, S., Pisso, I., Evangeliou, N., Zwaaftink, C. G., Plach, A., McConnell, J. R., Sigl, M., Ruppel, M., Zdanowicz, C., Lim, S., et al.: Revised historical Northern Hemisphere black carbon emissions based on inverse modeling of ice core records, Nature Communications, 14, 271, https://doi.org/10.1038/s41467-022-35660-0, 2023.

Edo, C., Gálvez-Blanca, V., González-Pleiter, M., Fernández-Piñas, F., and Rosal, R.: Microplastics in the cryosphere, in: Advances in Chemical Pollution, Environmental Management and Protection, vol. 13, pp. 245–268, Elsevier, https://doi.org/10.1016/bs.apmp.2025.10.001, 2025.

Enting, I. G.: Inverse problems in atmospheric constituent transport, Cambridge University Press, 2002.

Evangeliou, N., Grythe, H., Klimont, Z., Heyes, C., Eckhardt, S., Lopez-Aparicio, S., and Stohl, A.: Atmospheric transport is a major pathway of microplastics to remote regions, Nature communications, 11, 3381, https://doi.org/10.1038/s41467-020-17201-9, 2020.

Evangeliou, N., Tichý, O., Eckhardt, S., Groot Zwaaftink, C., and Brahney, J.: Sources and fate of atmospheric microplastics revealed from inverse and dispersion modelling; From global emissions to deposition, Journal of Hazardous Materials, 432, 128 585, https://doi.org/10.1016/j.jhazmat.2022.128585, 2022.

Evangelou, I., Tatsii, D., Bucci, S., and Stohl, A.: Atmospheric resuspension of microplastics from bare soil regions, Environmental Science & Technology, 58, 9741–9749, https://doi.org/10.1021/acs.est.4c01252, 2024.

Evangelou, I., Bucci, S., and Stohl, A.: Atmospheric microplastic emissions from land and ocean [Data set], Zenodo, https://doi.org/10.5281/zenodo.17660114, 2025.

Evangelou, I., Bucci, S., and Stohl, A.: Atmospheric microplastic emissions from land and ocean, Nature, pp. 1–4, https://doi.org/10.1038/s41586-025-09998-6, 2026.

Frank, Y. A., Tatsii, D., Rednikin, A. R., Plach, A., Rakhmatullina, S. N., Vorobiev, D. S., and Stohl, A.: It is snowing microplastics in Western Siberia, Environmental Pollution, 364, 125 293, https://doi.org/10.1016/j.envpol.2024.125293, 2025.

Fu, Y., Pang, Q., Ga, S. L. Z., Wu, P., Wang, Y., Mao, M., Yuan, Z., Xu, X., Liu, K., Wang, X., et al.: Modeling atmospheric microplastic cycle by GEOS-Chem: An optimized estimation by a global dataset suggests likely 50 times lower ocean emissions, One Earth, 6, 705–714, https://doi.org/10.1016/j.oneear.2023.05.012, 2023.

Ganesan, A. L., Rigby, M., Zammit-Mangion, A., Manning, A. J., Prinn, R. G., Fraser, P. J., Harth, C. M., Kim, K.-R., Krummel, P. B., Li, S., Mühle, J., O'Doherty, S. J., Park, S., Salameh, P. K., Steele, L. P., and Weiss, R. F.: Characterization of uncertainties in atmospheric trace gas inversions using hierarchical Bayesian methods, Atmospheric Chemistry and Physics, 14, 3855–3864, https://doi.org/10.5194/acp-14-3855-2014, 2014.

Gaston, E., Woo, M., Steele, C., Sukumaran, S., and Anderson, S.: Microplastics differ between indoor and outdoor air masses: insights from multiple microscopy methodologies, Applied spectroscopy, 74, 1079–1098, https://doi.org/10.1177/0003702820920652, 2020.

Goßmann, I., Herzke, D., Held, A., Schulz, J., Nikiforov, V., Georgi, C., Evangeliou, N., Eckhardt, S., Gerdts, G., Wurl, O., and Scholz-Bottcher, B.: Occurrence and backtracking of microplastic mass loads including tire wear particles in northern Atlantic air, Nature Communications, 14, 3707, https://doi.org/10.1038/s41467-023-39340-5, 2023.

Groot Zwaaftink, C., Arnalds, Ó., Dagsson-Waldhauserova, P., Eckhardt, S., Prospero, J., and Stohl, A.: Temporal and spatial variability of Icelandic dust emissions and atmospheric transport, Atmospheric Chemistry and Physics, 17, 10 865–10 878, https://doi.org/10.5194/acp-17-10865-2017, 2017.

https://doi.org/10.5194/egusphere-2026-5158
Preprint. Discussion started: 22 September 2026

Grythe, H., Ström, J., Krejci, R., Quinn, P., and Stohl, A.: A review of sea-spray aerosol source functions using a large global set of sea salt aerosol concentration measurements, Atmospheric Chemistry and Physics, 14, 1277–1297, https://doi.org/10.5194/acp-14-1277-2014, 2014.

Grythe, H., Kristiansen, N., Zwaaftink, C., Eckhardt, S., Ström, J., Tunved, P., Krejci, R., and Stohl, A.: A new aerosol wet removal scheme for the Lagrangian particle model FLEXPART, Geoscientific Model Development, 10, 1447–1466, https://doi.org/10.5194/gmd-10-1447-2017, 2017.

Harb, C., Pokhrel, N., and Foroutan, H.: Quantification of the emission of atmospheric microplastics and nanoplastics via sea spray, Environmental Science & Technology Letters, 10, 513–519, https://doi.org/10.1021/acs.estlett.3c00164, 2023.

Hersbach, H., Bell, B., Berrisford, P., Hirahara, S., Horányi, A., Muñoz-Sabater, J., Nicolas, J., Peubey, C., Radu, R., Schepers, D., et al.: The ERA5 global reanalysis, Quarterly Journal of the Royal Meteorological Society, 146, 1999–2049, https://doi.org/10.1002/qj.3803, 2020.

Hersbach, H., Bell, B., Berrisford, P., Biavati, G., Horányi, A., Muñoz Sabater, J., Nicolas, J., Peubey, C., Radu, R., Rozum, I., et al.: ERA5 hourly data on single levels from 1940 to present, Copernicus climate change service (c3s) climate data store (cds), 10, https://doi.org/10.24381/cds.adbb2d47, (Accessed on 13-05-2025), 2023.

Herzke, D., Schmidt, N., Lervik, A., Schulze, D., Celentano, S., Eckhardt, S., Arp, H. P. H., and Evangeliou, N.: Airborne microplastics on the move: Urban Europe as a source to remote regions, Environmental Pollution, p. 127380, https://doi.org/10.1016/j.envpol.2025.127380, 2025.

Huneeus, N., Schulz, M., Balkanski, Y., Griesfeller, J., Prospero, J., Kinne, S., Bauer, S., Boucher, O., Chin, M., Dentener, F., et al.: Global dust model intercomparison in AeroCom phase I, Atmospheric Chemistry and Physics, 11, 7781–7816, https://doi.org/10.5194/acp-11-7781-2011, 2011.

Isobe, A., Azuma, T., Cordova, M. R., Cózar, A., Galgani, F., Hagita, R., Kanhai, L. D., Imai, K., Iwasaki, S., Kako, S., et al.: A multilevel dataset of microplastic abundance in the world's upper ocean and the Laurentian Great Lakes, Microplastics and Nanoplastics, 1, 1–14, https://doi.org/10.1186/s43591-021-00013-z, 2021.

Jambeck, J. R., Geyer, R., Wilcox, C., Siegler, T. R., Perryman, M., Andrady, A., Narayan, R., and Law, K. L.: Plastic waste inputs from land into the ocean, science, 347, 768–771, https://doi.org/10.1126/science.1260352, 2015.

Jiang, F., Gao, C., Chan, A. W., Topping, D. O., Zhang, H., Li, W., Coe, H., Liu, X., Ching, J., and Zheng, Z.: A Review of Atmospheric Micro/Nanoplastics: Insights into Source and Fate for Modelling Studies, Current Pollution Reports, 11, 53, https://doi.org/10.1007/s40726-025-00375-5, 2025.

Jurkschat, L., Gill, A., Milner, R., Holzinger, R., Evangeliou, N., Eckhardt, S., and Materić, D.: Using a citizen science approach to assess nanoplastics pollution in remote high-altitude glaciers, Scientific Reports, 15, 1864, https://doi.org/10.1038/s41598-024-84210-9, 2025.

Kako, S., Isobe, A., and Kubota, M.: High-resolution ASCAT wind vector data set gridded by applying an optimum interpolation method to the global ocean, Journal of Geophysical Research: Atmospheres, 116, https://doi.org/10.1029/2010JD015484, 2011.

Kjærgaard, E. R., Hasager, F., Petters, S. S., Glasius, M., and Bilde, M.: Bubble-mediated generation of airborne nanoplastic particles, Environmental Science: Processes & Impacts, 26, 1216–1226, https://doi.org/10.1039/D4EM00124A, 2024.

https://doi.org/10.5194/egusphere-2026-5158
Preprint. Discussion started: 22 September 2026

Klimont, Z., Kupiainen, K., Heyes, C., Purohit, P., Cofala, J., Rafaj, P., Borken-Kleefeld, J., and Schöpp, W.: Global anthropogenic emissions of particulate matter including black carbon, Atmospheric Chemistry and Physics, 17, 8681–8723, https://doi.org/10.5194/acp-17-8681-2017, 2017.

Kye, H., Kim, J., Ju, S., Lee, J., Lim, C., and Yoon, Y.: Microplastics in water systems: A review of their impacts on the environment and their potential hazards, Heliyon, 9, https://doi.org/10.1016/j.heliyon.2023.e14359, 2023.

Lambert, S., Vercauteren, M., Catarino, A. I., Li, Y., Van Landuyt, J., Boon, N., Everaert, G., De Rijcke, M., Janssen, C. R., and Asselman, J.: Aerosolization of micro-and nanoplastics via sea spray: Investigating the role of polymer type, size, and concentration, and potential implications for human exposure, Environmental Pollution, 351, 124 105, https://doi.org/10.1016/j.envpol.2024.124105, 2024.

Latz, M., Gill, A., Evangeliou, N., Eckhardt, S., Milner, R., Reemtsma, T., and Materić, D.: Nanoplastic detection and quantification in high-altitude glacial snow samples from Italy, Switzerland and France, Scientific Reports, 16, 24 714, https://doi.org/10.1038/s41598-026-63263-y, 2026.

Leelőssy, Á., Mészáros, R., Kovács, A., Lagzi, I., and Kovács, T.: Numerical simulations of atmospheric dispersion of iodine-131 by different models, PloS one, 12, e0172 312, https://doi.org/10.1371/journal.pone.0172312, 2017.

Lehmann, M., Oehlschlägel, L. M., Häusl, F. P., Held, A., and Gekle, S.: Ejection of marine microplastics by raindrops: a computational and experimental study, Microplastics and Nanoplastics, 1, 18, https://doi.org/10.1186/s43591-021-00018-8, 2021.

Leslie, H., J. M. van Velzen, M., Brandsma, S., Vethaak, D., Garcia-Vallejo, J., and Lamoree, M.: Discovery and quantification of plastic particle pollution in human blood, Environment International, p. 107199, https://doi.org/10.1016/j.envint.2022.107199, 2022.

Li, Y., Zhang, J., Xu, L., Li, R., Zhang, R., Li, M., Ran, C., Rao, Z., Wei, X., Chen, M., et al.: Leaf absorption contributes to accumulation of microplastics in plants, Nature, pp. 1–8, https://doi.org/10.1038/s41586-025-08831-4, 2025.

Ling, Y., Yue, Q., Huang, T., Shan, Q., Hei, D., Zhang, X., and Jia, W.: Multi-nuclide source term estimation method for severe nuclear accidents from sequential gamma dose rate based on a recurrent neural network, Journal of Hazardous Materials, 414, 125 546, https://doi.org/10.1016/j.jhazmat.2021.125546, 2021.

Lobell, D. B., Schlenker, W., and Costa-Roberts, J.: Climate trends and global crop production since 1980, Science, 333, 616–620, https://doi.org/10.1126/science.1204531, 2011.

Marvel, K., Su, W., Delgado, R., Aarons, S., Chatterjee, A., Garcia, M. E., Hausfather, Z., Hayhoe, K., Hence, D. A., Jewett, E. B., Robel, A., Singh, D., Tripati, A., and Vose, R. S.: Climate Trends, in: Fifth National Climate Assessment, chap. 2, U.S. Global Change Research Program, Washington, DC, USA, https://doi.org/10.7930/NCA5.2023.CH2, 2023.

Masry, M., Rossignol, S., Roussel, B. T., Bourgogne, D., Bussière, P.-O., R'mili, B., and Wong-Wah-Chung, P.: Experimental evidence of plastic particles transfer at the water-air interface through bubble bursting, Environmental Pollution, 280, 116 949, https://doi.org/10.1016/j.envpol.2021.116949, 2021.

Oehlschlägel, L. M., Schmid, S., Lehmann, M., Gekle, S., and Held, A.: Water–air transfer rates of microplastic particles through bubble bursting as a function of particle size, Microplastics and Nanoplastics, 4, 1, https://doi.org/10.1186/s43591-023-00079-x, 2024.

Pingali, P. L.: Green revolution: impacts, limits, and the path ahead, Proceedings of the national academy of sciences, 109, 12 302–12 308, https://doi.org/10.1073/pnas.0912953109, 2012.

https://doi.org/10.5194/egusphere-2026-5158
Preprint. Discussion started: 22 September 2026

Plastics Europe: Plastics—the Facts 2024, (Plastics Europe, accessed 10.09.2025), 2024.

Pokhrel, N. and Foroutan, H.: Effect of wettability on microplastic aerosolization via film and jet drops ejected from bursting bubbles, Environmental Science: Processes & Impacts, https://doi.org/10.1039/D5EM00876J, 2026.

Potapov, P., Turubanova, S., Hansen, M. C., Tyukavina, A., Zalles, V., Khan, A., Song, X.-P., Pickens, A., Shen, Q., and Cortez, J.: Global maps of cropland extent and change show accelerated cropland expansion in the twenty-first century, Nature Food, 3, 19–28, https://doi.org/10.1038/s43016-021-00429-z, 2022.

Primpke, S., Fischer, M., Lorenz, C., Gerdts, G., and Scholz-Böttcher, B.: Comparison of pyrolysis gas chromatography/mass spectrometry and hyperspectral FTIR imaging spectroscopy for the analysis of microplastics, Analytical and Bioanalytical Chemistry, 412, 8283–8298, https://doi.org/10.1007/s00216-020-02979-w, 2020.

Ray, D. K., Ramankutty, N., Mueller, N. D., West, P. C., and Foley, J. A.: Recent patterns of crop yield growth and stagnation, Nature communications, 3, 1293, https://doi.org/10.1038/ncomms2296, 2012.

Ray, D. K., Mueller, N. D., West, P. C., and Foley, J. A.: Yield trends are insufficient to double global crop production by 2050, PloS one, 8, e66 428, https://doi.org/10.1371/journal.pone.0066428, 2013.

Richon, C., Gorgues, T., Paul-Pont, I., and Maes, C.: Zooplankton exposure to microplastics at global scale: Influence of vertical distribution and seasonality, Frontiers in Marine Science, 9, 947 309, https://doi.org/10.3389/fmars.2022.947309, 2022.

Ryan, A. C., Allen, D., Allen, S., Maselli, V., LeBlanc, A., Kelleher, L., Krause, S., Walker, T. R., and Cohen, M.: Transport and deposition of ocean-sourced microplastic particles by a North Atlantic hurricane, Communications Earth & Environment, 4, 442, https://doi.org/10.1038/s43247-023-01115-7, 2023.

Saha, S. C. and Saha, G.: Effect of microplastics deposition on human lung airways: A review with computational benefits and challenges, Heliyon, 10, https://doi.org/10.1016/j.heliyon.2024.e24355, 2024.

Seibert, P. and Frank, A.: Source-receptor matrix calculation with a Lagrangian particle dispersion model in backward mode, Atmospheric Chemistry and Physics, 4, 51–63, https://doi.org/10.5194/acp-4-51-2004, 2004.

Shaw, D. B., Li, Q., Nunes, J. K., and Deike, L.: Ocean emission of microplastic, PNAS nexus, 2, pgad296, https://doi.org/10.1093/pnasnexus/pgad296, 2023.

Su, Y., Gabrielle, B., and Makowski, D.: A global dataset for crop production under conventional tillage and no tillage systems, Scientific Data, 8, 33, https://doi.org/10.1038/s41597-021-00817-x, 2021.

Tarantola, A.: Inverse problem theory and methods for model parameter estimation, SIAM, 2005.

Tatsii, D., Bucci, S., Bhowmick, T., Guettler, J., Bakels, L., Bagheri, G., and Stohl, A.: Shape matters: long-range transport of microplastic fibers in the atmosphere, Environmental science & technology, 58, 671–682, https://doi.org/10.1021/acs.est.3c08209, 2023.

Tichý, O., Ulrych, L., Šmídl, V., Evangeliou, N., and Stohl, A.: On the tuning of atmospheric inverse methods: comparisons with the European Tracer Experiment (ETEX) and Chernobyl datasets using the atmospheric transport model FLEXPART, Geoscientific Model Development, 13, 5917–5934, https://doi.org/10.5194/gmd-13-5917-2020, 2020.

Trainic, M., Flores, J., Pinkas, I., Pedrotti, M., Lombard, F., Bourdin, G., Gorsky, G., Boss, E., Rudich, Y., Vardi, A., et al.: Airborne microplastic particles detected in the remote marine atmosphere, Communications Earth & Environment, 1, 64, https://doi.org/10.1038/s43247-020-00061-y, 2020.

https://doi.org/10.5194/egusphere-2026-5158
Preprint. Discussion started: 22 September 2026

Vojta, M., Plach, A., Annadate, S., Park, S., Lee, G., Purohit, P., Lindl, F., Lan, X., Mühle, J., Thompson, R. L., et al.: A global re-analysis of regionally resolved emissions and atmospheric mole fractions of SF6 for the period 2005–2021, Atmospheric Chemistry and Physics, 24, 12 465–12 493, https://doi.org/10.5194/acp-24-12465-2024, 2024.

Wang, Q., Li, J., Zhu, X., Sun, C., Teng, J., Chen, L., Shan, E., and Zhao, J.: Microplastics in fish meals: An exposure route for aquaculture animals, Science of the Total Environment, 807, 151 049, https://doi.org/10.1016/j.scitotenv.2021.151049, 2022.

Xu, S., Zhao, R., Sun, J., Sun, Y., Xu, G., and Wang, F.: Microplastics change soil properties, plant performance, and bacterial communities in salt-affected soils, Journal of Hazardous Materials, 471, 134 333, https://doi.org/10.1016/j.jhazmat.2024.134333, 2024.

Yang, S., Zhang, T., Gan, Y., Lu, X., Chen, H., Chen, J., Yang, X., and Wang, X.: Constraining microplastic particle emission flux from the ocean, Environmental Science & Technology Letters, 9, 513–519, https://doi.org/10.1021/acs.estlett.2c00214, 2022.

Yang, S., Brasseur, G., Walters, S., Lichtig, P., and Li, C. W.: Global atmospheric distribution of microplastics with evidence of low oceanic emissions, npj Climate and Atmospheric Science, 8, 81, https://doi.org/10.1038/s41612-025-00914-3, 2025.

Zhang, Y., Gao, T., Kang, S., Allen, D., Wang, Z., Luo, X., Yang, L., Chen, J., Hu, Z., Chen, P., et al.: Cryosphere as a temporal sink and source of microplastics in the Arctic region, Geoscience Frontiers, 14, 101 566, https://doi.org/10.1016/j.gsf.2023.101566, 2023.